HHS Public Access

Author manuscript

*Nature*. Author manuscript; available in PMC 2020 October 15.

Published in final edited form as:

*Nature*. 2020 April ; 580(7805): 658–662. doi:10.1038/s41586-020-2186-z.

# Action of a minimal contractile bactericidal nanomachine

**Peng Ge**[a,b,*], **Dean Scholl**[d,*], **Nikolai S. Prokhorov**[g], **Jaycob Avaylon**[b,c], **Mikhail M. Shneider**[e], **Chris Browning**[f], **Sergii A. Buth**[g], **Michel Plattner**[g], **Urmi Chakraborty**[d], **Ke Ding**[a,b], **Petr G. Leiman**[g], **Jeff F. Miller**[a,b,%], **Z. Hong Zhou**[a,b,%]

[a]Department of Microbiology, Immunology and Molecular Genetics, University of California, Los Angeles (UCLA), Los Angeles, CA 90095, USA

[b]The California NanoSystems Institute (CNSI), University of California, Los Angeles (UCLA), Los Angeles, CA 90095, USA

[c]Department of Chemistry and Biochemistry University of California, Los Angeles (UCLA), Los Angeles, CA 90095, USA

[d]Pylum Biosciences, 100 Kimball Way, S. San Francisco, CA 94080, USA

[e]Shemyakin-Ovchinnikov Institute of Bioorganic Chemistry, Laboratory of Molecular Bioengineering, 16/10 Miklukho-Maklaya St., 117997, Moscow, Russia

[f]Vertex Pharmaceuticals (Europe) Ltd, Abingdon, Oxfordshire OX14 4RW, UK

[g]University of Texas Medical Branch, Department of Biochemistry and Molecular Biology, Sealy Center for Structural Biology and Molecular Biophysics, 301 University Blvd, Galveston, TX 77555-0647, USA

## Abstract

R-type bacteriocins are minimal contractile nanomachines that hold promise as precision antibiotics[1–4]. Each bactericidal complex uses a collar to bridge a hollow tube with a contractile sheath loaded in a metastable state by a baseplate scaffold[1,2]. Fine-tuning of such nucleic acid-free protein machines for precision medicine calls for an atomic description of the entire complex and contraction mechanism, which is not available from baseplate structures of (DNA-containing) T4 bacteriophage5. Here we report the atomic model of the complete R2 pyocin in its pre- and post-contraction states, each containing 384 subunits of 11 unique atomic models of 10 gene products.



% Correspondence should be addressed to J.F.M. (jfmiller@ucla.edu) or Z.H.Z. (Hong.Zhou@UCLA.edu).

*These authors contributed equally.

Author Contributions

Z.H.Z., J.F.M., P.G. and P.G.L. conceived the project; D.S., J.A. and K.D. prepared pyocin R2 samples used for high resolution cryoEM; P.G. and J.A. recorded the cryoEM data; P.G. and Z.H.Z. processed the cryoEM data; P.G., J.A. and P.G.L. built the atomic models using cryoEM data; P.G., P.G.L., J.A. and Z.H.Z. analyzed and interpreted the models; D.S., N.S.P. and U.C. created pyocin mutants and examined their assembly properties and phenotypes; N.S.P. designed functional assays and CD experiments to measure the activation energy of sheath contraction; M.M.S. created the expression constructs used for crystallography; C.B. and P.G.L. determined the crystal structure of the PA0616 spike protein; S.B. and M.P. determined the crystal structure of the C-terminal domain of PA0618; P.G., Z.H.Z., J.A., P.G.L., D.S. and J.F.M. wrote the paper; and all authors contributed to the editing of the manuscript.

Competing Interests

J.F.M. is a cofounder, equity holder, and a member of the Board of Directors of Pylum Biosciences, Inc., a biotherapeutics company in South San Francisco, USA. D.S is an equity holder of the same company.

Comparison of these structures suggests the sequence of events during pyocin contraction: tail fibers trigger lateral dissociation of baseplate triplexes; the dissociation then initiates a cascade of events leading to sheath contraction; this contraction converts chemical energy into mechanical force to drive the iron-tipped tube across the bacterial cell surface, killing the bacterium.

Contractile nanotube-based machines are widespread in the bacterial domain, functioning to penetrate cell membranes to deliver payloads of proteins or DNA, or to create channels through which ions translocate[6]. Contractile type VI secretion systems (T6SS) inject proteins into eukaryotic or bacterial cells to facilitate pathogenesis or kill competing organisms, respectively[7–13]. Phage tail-like bacteriocins, exemplified by R-type pyocins produced by *Pseudomonas aeruginosa,* employ the same contractility to kill competing bacteria by dissipating their membrane potential[1,2,14]. Myovirus bacteriophages, such as P2 and T4, use a similar contractile mechanism to translocate DNA into bacterial cells[5,9,15–22]. These contractile nanomachines employ a spring-loaded sheath-tube assembly to penetrate target cell surfaces[11]. This process is accompanied by massive structural transformations involving contraction of the sheath triggered by the baseplate, which has been visualized both by single-particle cryo-electron microscopy (cryoEM)[1,7,10,23,24] and by cellular cryo-electron tomography[25]. Although energy storage is mostly similar in phage, pyocin and T6SS, the triggering mechanism may be different, due to the presence of additional cell membranes in the case of T6SS. In contrast, some other delivery systems, such as the type III and IV secretion systems[26,27] carry no stored energy for penetration or baseplate-like structure for triggering.

An engineered T4 tube-baseplate complex reported previously[5] shows the static structures of baseplate proteins but lacks the sheath to inform how it receives the contraction signal. More recently, cryoEM structures of insecticidal contractile toxin-delivery systems from *Photorhabdus asymbiotica* (*Photorhabdus* virulence cassette[23]), and *Serratia entomophila* (antifeeding prophage[24]), showcase the widespread existence of such phage tail-like contractile systems in nature. The relative simplicity and ease of engineering[3,4] of R-type pyocins make them ideal model systems for studying contractile structures. Our previous helical reconstructions of the pyocin R2 sheath and tube in pre- and post-contraction states[1] revealed how energy for contraction is stored and released by shape and charge complementarity. The lack of atomic detail on the baseplate and collar, however, precluded understanding the molecular trigger that initiates sheath contraction, or how the resulting structure is stabilized to facilitate killing.

Here, we report the atomic models of pyocin collar and baseplate derived from single-particle cryoEM and X-ray crystallography in their pre- and post-contraction states. By comparing these structures, we derived and tested a model for the action of a bactericidal nanomachine that couples specific recognition of target cells with deployment of a generic mechanism of killing, providing insights crucial for exploiting these structures as precision antimicrobials[2,28,29].

## Overall structures of pyocin R2

We imaged pyocin R2 by cryoEM (Fig. 1a,b). Under the conditions used for sample isolation, both pre- and post-contracted particles are present in the same preparation[1]. Each pyocin R2 complex consists of three structurally and functionally distinct components: collar, trunk and baseplate with tail fibers. In the post-contracted state, the sheath layer of the trunk contracts 70%, leaving the central tube exposed and readily visible in the cryoEM images (Fig. 1a,b). We determined the cryoEM structures of pre-contraction pyocin R2 collar, trunk and baseplate regions separately and made a montage model by computationally stitching the three parts together (Fig. 1a,b, Supplementary Video 1). Substructures were determined at resolutions of 3.8 Å for the collar, 2.9 Å for the trunk, and 3.5 Å for the baseplate (Extended Data Fig. 1–2, Extended Data Table 1). Though the average resolution of the baseplate reaches 3.5 Å (Fig. 1c, Supplementary Video 2), the resolution of the peripheral regions is lower, possibly due to blurring from Brownian motion of the connected tail fibers. [These regions are modeled according to both their cryoEM density and our crystal structure of an engineered protein representing them (PDB:5CES) (Extended Data Table 2).] Using the same strategy, we determined the structure of the post-contraction pyocin at intermediate resolutions (Fig. 1a, right, Supplementary Video 3). By matching amino acid side chains visible in our cryoEM structures, we assigned a single gene product, PA0615, to the collar, 2 gene products, PA0622–0623 to the trunk (PA0622 sheath and PA0623 tube), and 7 gene products, PA0616–0619 and PA0626–0628, to the various components of the baseplate and built an atomic model for the complete pyocin, excluding tail fiber and tape measure proteins (PA0620 and PA0625, respectively) (Fig. 1d–f, Supplementary Video 4, Extended Data Table 3).

## Collar tethers tube to the contracted sheath

The collar is a hexamer formed by gene product PA0615 (Fig. 2a,b). Each collar monomer has a simple structure with two domains, one globular domain and one β-hairpin domain, joined by an extended loop (Fig. 1e, 2b). The structure of the globular domain is similar to that of the inner tube protein. The collar extends the tube and tethers it to the sheath, thus preventing the tube from dissociating from the sheath after contraction as demonstrated in *Photorhabdus* virulence cassette[23]. By capping the top of the tube and augmenting the *handshake* β-sheet of the sheath subunit below with a β-hairpin (similar to the sheath-sheath handshake[1,7,10]), it provides mechanical stability to the junction after the downward pull of the sheath against the tube (Fig. 2a,b).

Specifically, the handshake domain of each sheath subunit is augmented by two β-strands that are donated by subunits from a disk that is closer to the collar. Each subunit of the last disk thus has a β-sheet with two vacant β-strands. The β-hairpin domain of the collar protein completes this β-sheet. In addition, the hydrogen bond interactions in this augmentation are reinforced by charge-charge interactions: the loop and the β-hairpin domain of the collar is mainly negative, binding to a groove in the sheath that is mainly positive (Fig. 2c), unlike the very hydrophobic nature of the sheath-sheath interaction. In this configuration, the collar hexamer joins the tube and the sheath at the very top.

We also determined the structure of the post-contraction collar region at an average resolution of 3.5 Å (Extended Data Fig. 1). The most dramatic structural change is that the diameter of the outer sheath increases from 180Å to 240Å, resulting in the dislocation of the sheath from the tube (Fig. 2d). This dislocation appears to reduce the structural rigidity of the collar protein linker and increase local mobility of the tube, as the averaged resolution of the tube portion in the reconstruction is only 7Å and the linker has become invisible. Nonetheless, the rest of the structure, including the sheath protein and the hairpin domain of the collar, is of sufficient resolution for building atomic models. The hairpin domain of the collar undergoes a slight conformational change during contraction, but the globular domain remains structurally unchanged.

## Trunk and the sheath initiator

Since we determined the structures of the bottommost part of the trunk and the baseplate without imposing helical symmetry, we can now resolve the interface regions of both components. Six subunits of the PA0623 *tube* protein form a hexameric ring with a 24-stranded β -barrel, 28 of which stack into the central tube of each pyocin. Handshake interactions with long N- and C-terminal extension arms interweave PA0622 *sheath* protein subunits, maintaining the connectivity of the sheath during contraction (Extended Data Fig. 3). Thus our new non-helical structure confirms our previous observations based on helical reconstructions of the trunk portion of pyocin from images recorded on films[1].

Sheath disks approaching the baseplate break from the shared helical symmetry of the trunk with a slightly but gradually increasing rotation per disk, reaching 4.4 extra degrees in the bottommost disk (Extended Data Fig. 4). The handshake β-sheet is the same across the entire sheath, except for the bottommost disk where sheath subunit arms are incorporated into the PA0617 *sheath initiator* protein (Extended Data Fig. 3). The arm of the sheath protein augments a β-sheet of the sheath initiator protein in the same manner as in the rest of the sheath. Thus, the β-sheet augmentation mechanism allows the sheath to be linked via multiple polypeptide chains both to the collar and to the baseplate. (See three different kinds of handshaking augmentation in Extended Data Fig. 3.)

## Baseplate: triggering triplex and ripcord

Our reconstruction shows that pyocin baseplate is composed of eight different protein subunits: *ripcord* (PA0626), *triplex* [two copies of PA0618 (*Tri1a* and *Tri1b*) and one copy of PA0619 (*Tri2*)], sheath initiator (PA0617), *glue* (PA0627), *hub* (PA0628) and *spike* (PA016) (Fig. 1e, Extended Data Fig. 5). PA0626 forms the centerpiece of the baseplate (Extended Data Fig. 5a): the central spike complex is ‘below’, the tube/sheath and the trunk they form is ‘above’, and the rest of the baseplate (triplex, sheath initiator and glue) surrounds it. The central spike complex is composed of the trimeric/pseudo-hexameric PA0628 hub (Extended Data Fig. 5b) and the trimeric PA0616 central spike inserted into it (Extended Data Fig. 5c). Our crystal structure of the PA0616 spike, a homologue of P2 phage gpV[30], shows that it carries a ferric ion at the very tip. The ferric ion is coordinated by a triplet of HxH double histidine motifs, a structure that stabilizes the tip for membrane penetration (Extended Data Fig. 5c).

Each PA0626 monomer has a C-terminal β-sheet domain (aa. 136–286) and an N-terminal helix-rich domain (aa. 1–112) joined by an extended linker (aa. 113–135) – an unusual domain organization reminiscent of a *ripcord* (Extended Data Fig. 5a). We reason that this setup may comprise a form of activation energy barrier for triggering and may also be crucial for assembly: The C-terminal domains of six PA0626 subunits form a hexameric disk which resembles that of the tube proteins and extends the tube (Extended Data Fig. 5a). This disk is integral to the tube-PA0626-hub-spike assembly that penetrates the target as it connects the tube to the hub. The N-terminal domains of PA0626, a four-helical bundle structure, are localized at higher cylindrical radius inside the baseplate (Extended Data Fig. 5d). Indeed, when we introduce a TEV protease cleavage site in the linker of the ripcord, the mutant pyocin (626TEV) shows wildtype-like assembly without TEV protease co-expressed and no assembly with TEV protease co-expressed (Extended Data Fig. 6). We also found that this mutant (626TEV) and another deletion mutant (626ΔWL) have lower activation energy for triggering compared to wildtype (Extended Data Fig. 6).

Two copies of PA0618 and one copy of PA0619 proteins form a $(PA0618)_2$-PA0619 heterotrimeric *triplex* by attaching two copies of PA0618 (*tri1a/b*) to either side of PA0619 (*tri2*), resulting in two distinct conformations of PA0618 (Extended Data Fig. 7), which accept the PA0626 N-terminal four helical bundle domain (Extended Data Fig. 8). This triplex also binds at its top the sheath initiator PA0617 protein. A small protein with a LysM fold – PA0627 – binds to a side of the triplex and *glues* PA0617, PA0618b and PA0619 together (Extended Data Fig. 5e). The $(PA0618)_2$-PA0619 triplexes are joined into an iris-like structure by lateral dimers of the C-terminal domains of PA0618 (Fig. 3a, Extended Data Fig. 7e,f). PA0619 attaches to the tail fiber, allowing it to receive a triggering signal from it (Extended Data Fig. 5f).

By comparing the pre- and post-contraction baseplate models, we found that the “iris-ring”[5], joined by lateral dimerization of PA0618, break apart after contraction of the pyocin (Fig. 1d and Fig. 3). In this way, the baseplate in the post-contraction state splits into a hexagram shape. The entire complex of sheath initiator, glue and triplex travels in a rigid-body movement as each sheath subunit does, widening the baseplate to 320 Å (Fig. 3b). The tail fiber still binds to the triplex upon contraction, as its densities are still visibly connected to the triplex, although at low resolution.

Compared to the bacteriophage T4 baseplate[5], pyocin baseplate proteins are minimalistic and bear interesting differences. PA0618 and PA0619 both lack sizeable insertion domains required for building the considerably larger T4 baseplate. Instead, these insertions are replaced by loops (Extended Data Fig. 9), although their function as struts that connect hub and baseplate is preserved. PA0617 and PA0627 are also minimal compared to T4 gp25 and gp53, respectively, simply retaining the core motifs[5] (Extended Data Fig. 9). Furthermore, the pyocin sheath protein lacks domains 3 and 4 of the T4 sheath protein, which add to the energy release of contraction and interact with long tail fibers, respectively[16,17].

## Bactericidal action and application

Based on our atomic models of R2 pyocin in pre- and post-contracted states, we constructed a *minimal* contractile machine that includes just twelve stacks of sheath and rendered a morph movie between the two states to illustrate a possible pathway of action of such a contractile nano-machine (Supplementary Video 5). Notably, because the sheath changes helicity during contraction, the tube undergoes a rotational movement during its power stroke which may facilitate spike's penetration of the target cell surface.

The biological function of R-type pyocins is to kill competing bacteria and they do so with an extraordinary efficiency that approaches single-shot killing[4,31]. To achieve this it is necessary to actuate only in the right place and time. Upon recognition by tail fiber receptor binding proteins of specific ligands on a target cell, the increased free energy would cause displacement of interacting surfaces within lateral dimers of PA0618, and we suggest that shearing forces transduced through tail fibers trigger the baseplate to initiate contraction (Fig. 4). Shearing force encountered by particles during purification may bear similar characteristics. This force drives the baseplate to transit to a larger diameter, breaking lateral dimers of PA0618 Tri1a/b (Fig. 3a–f). This process may be reversible to a threshold level, ensuring that a sufficient number of tail fiber binding interactions occurs to disrupt enough lateral dimers to break the triplex iris ring and begin the irreversible process of sheath contraction[32]. This would provide a "checksum" mechanism for the baseplate and avoid premature triggering. It may also be used to ensure that the pyocin is positioned upright to prevent sideward, non-productive firing, since the arrangement of triggering tail fibers may also play a role in setting off the baseplate[32] (Fig. 4a). As the iris breaks, the triplexes may pull the four-helical bundles of attached ripcord proteins, lowering the final barrier to contraction (Fig. 4).

Indeed, changing the lateral dimer interface between PA0618 Tri1a/b subunits alters the firing characteristics of pyocin. Due to the presence of a histidine residue in the interface, pyocins are sensitive to acidic environment and their contraction is triggered by pH 3.4 (Fig. 3g), at which the histidine is protonated to disturb the dimer interface (Fig. 3f). We engineered a mutant, H257F, in which the histidine is replaced by a phenylalanine. We found that the mutant is more tolerant to acid than the wildtype (WT) pyocin: whereas cryoEM images show that purified WT and H257F both contain similar percentage of pre-contraction pyocins at neutual pH (64% and 67%, respectively); at pH 3.4, however, cryoEM images show that far more WT than H257F pyocins have been triggered into post-contraction state (9% and 36% of remaining pre-contraction pyocins, respectively) (Fig. 3g). Two other PA0618 mutations at the lateral dimer interface, S250A and A254C (see Fig. 3f), resulted in either defective assembly (S250A) or premature firing (A254C) of the particles.

Among the known structures of similar contractile systems, sheath and sheath initiator are both conserved, indicating that key aspects of the contraction mechanism are conserved[6,8]. Whether these similarities extend also to T6SS baseplate proteins is not known in the absence of atomic structures. Thus far, however, the four-helix bundle motif of the ripcord protein described here seems to be unique to pyocin R2 and related phages (e.g., PS17 phage) based on genetic information. Indeed, a search in other contractile tail-like systems

did not yield any four-helix bundle orthologs, though all contain orthologs for the triplex proteins. This unique triggering system puts pyocin R2 in a special position among contractile structures, perhaps due to its minimal nature that precludes sophisticated and sizeable insertion domains like those of T4.

R-type pyocins and related R-type bacteriocins are being developed as a new class of antimicrobials[2–4,28,29]. A unique feature of these structures is that highly specific target recognition conferred by RBPs is directly coupled to the mechanism of action. This exquisite specificity allows selective killing of pathogens without the unintended consequences of off-target effects such as dysbiosis[33], and without selecting for transmissible antibiotic resistance in off-target bacterial species or strains. Engineering RBPs to alter R-type pyocin binding specificity has already been demonstrated[3,4,34]. We now have the information required to fine tune the triggering mechanism through structure-guided alterations at key interaction points between baseplate components. For applications that require precise ablation of pathobionts from complex bacterial ecosystems, a less sensitive trigger would minimize off-target effects, and only set off the killing mechanism when tightly bound to the correct bacterial cell. On the other hand, in full blown infections such as septicemia, where a single pathogen has grown to high density, a more sensitive trigger would allow for more efficient killing upon collision with the target. The adaptability of contractile injection systems and the modularity of receptor binding proteins, both honed over eons of evolution, provide an opportunity to engineer precision antibiotics for human and animal health.

## Methods

### Purification of pyocins for cryoEM

Pyocin sample was prepared from *pseudomonas aeruginosa* strain PAO1 as previously described[1,4]. Briefly, a crude pyocin sample was first prepared from PAO1 and harvested by high-salt precipitation and differential centrifugation. This crude sample was further purified using a 10% to 50% sucrose (w/v) gradient at 77,000g for 1.5 hours at 4°C. After centrifugation, one band was visible at about 25% position and was extracted gently by fractionation with a 100 μL pipette from the top of the centrifuge tube along its side. The extracted sample was then diluted to a final volume of 4mL with Tris buffer (10 mM Tris, 130 mM NaCl, pH 7.4). The diluted sample was concentrated using a 100kDa Amicon molecular filter to about 50 μL. This dilution-concentration step was repeated 3 more times in the same filter as a means of dialysis, ending up with a final sample volume of 50 μL for cryoEM imaging.

### Cloning and purification of proteins for crystallography

Bioinformatic analysis with the help of HHpred[35] was used to identify the P. aeruginosa PAO1 genes encoding the central spike protein (PA0616) and Tri1 (PA0618) in the R2 pyocin cluster of *Pseudomonas aeruginosa* PAO1. The proteins were amplified with the primers given in the Supplementary Table 1. *Pa0616* was cloned into the pEEv3 vector (a pET23d derivative with a TEV proteinase cleavage site downstream from the N-terminal His-Tag) using the BamHI and HindIII restriction sites. PA0618 was cloned into the

standard pET23 using the NdeI and XhoI restriction sites to give rise to a protein with a non-cleavable C-terminal His-tag.

Both proteins were expressed in *E. coli* B834 (DE3) cells grown in 2xTY medium at 37° C and aerated at 200 rpm to $OD_{600}$ 0.6 and induced with the addition of 1 mM IPTG. The temperature of the culture was lowered to 18°C and protein expression was carried overnight. The cells were pelleted by centrifugation for 10 min at 8,000×g at 4C and then lysed by sonication. The soluble fraction was separated by centrifugation for 15 min at 25,000×g at 4C and loaded on the IMAC resin (GE HealthScience). The IMAC affinity chromatography was performed in 10 mM TrisCl pH 8.0 with a 0–300 mM imidazole gradient. Fractions containing the protein were dialyzed into 10 mM TrisCl pH 8.0 overnight. The TEV protease in a 1/10 mass-to-mass ratio (TEV protease/target protein) was added to the PA0616 sample, and proteolysis of the N-terminal His-tag was performed simultaneously with a dialysis into 10 mM TrisCl pH 8.0 overnight at room temperature. The dialysis of PA0618 was performed overnight at +4°C. The subsequent steps of protein purification were the same for both proteins. The samples were loaded onto a MonoQ 10/100 GL column equilibrated with a 10 mM TrisCl pH 8.0 and eluted with a 0–1 M NaCl gradient. Fractions containing the proteins of interest were then subject to size exclusion chromatography on a Superdex 200 10/300 GL column in the buffer 10 mM TrisCl pH 8.0, 150 mM NaCl. Fractions containing the proteins were pooled together and concentrated while the buffer was changed to 20 mM Tris Cl pH 8.0.

## Crystallization and structure determination of PA0616 and PA616d

For crystallization, PA0616 is concentrated to 18 mg/ml and subjected to a sparse matrix random screen using crystallization kits produced by Jena BioSciences. Best crystals of PA0616 were obtained in 60% PEG-400, 100 mM $Na_2SO_4$, 100 mM Bis-Tris buffer at pH 8.5 in hanging drop. A number of datasets were collected at the beamlines PX-I and PX-III of the Swiss Light Source (SLS) and the best dataset was used in structure refinement (Extended Data Table 2). The crystals did not require a special cryoprotectant and could be flesh frozen directly from the drop.

The structure of PA0616 was solved by molecular replacement using P2 phage gpV[30] as a search model (the two proteins display 31% sequence identity). The PA0616 unit cell contained 6 trimers in the asymmetric unit. The gpV search model contained the OB-fold and the first three strands of the beta-helix. The initial solution was found with the help of Molrep[36]. It was rigid body refined with Refmac5 (Ref. 37). Ten cycles of density modification by solvent flattening and non-crystallographic averaging with Parrot[38] improved the density to a point where the OB-fold and the first three beta-strands could be interpreted in terms of PA0616 amino acids. A new model of one chain was then superimposed onto the other 17 chains comprising the asymmetric unit. A new round of rigid body refinement was performed with Refmac5 (Ref. 37). The new density was subjected to additional 15 cycles of solvent flattening and non-crystallographic averaging with Parrot. The new map was interpretable throughout and the model could be built for all but the last five amino acids, comprising the Fe-binding site. This region of the model was disordered in all other datasets of PA0616 (including different space groups).

To reveal the structure of the Fe-binding site, we designed a shortened mutant of PA0616 (called PA0616d) that comprised 90 C-terminal residues (amino acids 96–185) of the full-length protein. PA0616d was PCR-amplified using primers given in the Supplementary Table 1 and cloned into pEEv3 so that it carried a cleavable His-tag at its N-terminus. The expression and purification was performed in a way similar to the full-length protein. PA0616d was then concentrated to 15 mg/ml and subjected to a sparse matrix random screen using crystallization kits produced by Jena BioSciences. Best crystals of PA0616d were obtained in 34% PEG-400, 200 mM $Na_2SO_4$, 100 mM Na-Acetate buffer at pH 5.0 in hanging drop. The crystals did not require a special cryoprotectant and could be flesh frozen directly from the drop. The crystallographic data were collected at the beamline PX-I of the SLS. The structure was solved by molecular replacement using the middle part of the overlapping fragment (residues 120–179) of the full-length PA0616 with the help of the Phaser program[39]. The N-terminal part of PA0616d beta-helix was significantly different to that of the full-length. Instead of forming a compact structure, it was splayed out and opened like a flower. This structural difference made structure solution difficult, but thanks to the availability of very high-resolution data (Extended Data Table 2) after several rounds of model building and refinement coupled to density modification with Parrot, an interpretable density could be obtained for the rest of the protein (including the Fe-binding site).

The structures of PA0616 and PA0616d were refined with Coot[40], Refmac5 (Ref. 37) and Phenix[41]. The final models of PA0616 and PA0616d were deposited to the Protein Data Bank under the accession numbers 4S37 and 4S36, respectively.

## Production of PA0618 fragment suitable for crystallographic analysis and the solution of the structure

Full-length PA0618 failed to crystallize. We, therefore, subjected it to limited proteolysis by trypsin. Full-length PA0618 was digested with trypsin (trypsin:PA0618 ratio of 1:500) in high salt buffer (20 mM Tris pH 8.0, 400 mM NaCl, 4 mM $CaCl_2$) for 75 minutes at room temperature. The reaction was quenched by the addition of PMSF to a final concentration of 2mM. This procedure resulted in two stable fragments. We loaded the mixture onto a His-Trap column (GE) and found that one of the fragments bound to the resin, suggesting that this fragment retained the His-tag and therefore constituted a C-terminal part of the protein (PA0618C). The fragment eluted from the column with a 10 mM Tris pH 8.0 buffer containing imidazole at 250 mM. The eluted protein was further purified by size exclusion chromatography (Superdex 75 HiLoad 16/60), dialyzed into 20 mM Tris pH 8.0, 5 mM DTT overnight and then purified by anion exchange chromatography (Mono Q 10/100). Fractions comprising the elution peak were pooled and purified by size exclusion chromatography (Superdex 75 HiLoad 16/60, 10mM Tris pH:8.0, 150mM NaCl) again. Purified PA0618 C-terminus was concentrated to 40 mg/ml and screened for crystallization conditions using Jena BioSciences crystallization kits. Crystallization drops of the best crystallization condition carried a crust, which prevented optimal crystal growth. Lowering of protein concentration prevented the formation of the crust, but it also stopped crystal formation. Best crystals were obtained by streak seeding of drops containing PA0618C at 17 mg/ml and 17% PEG 5000 MME, 150 mM $NH_4CH_3CO_2$, 100 mM MES pH 6.5.

Crystallographic data was collected at SLS beamlines PX-I and PX-III using well solution supplemented with 25% ethylene glycol as a cryoprotectant. The initial phases were obtained by a single wavelength anomalous diffraction technique (SAD) using $HoCl_2$ heavy atom derivative. The crystals were soaked in the well solution containing $HoCl_2$ at 5 mM for 24 hours. The model comprising residues 202–295 plus a His-tag was initially built by buccaneer[42] and completed manually. The structure of a better native dataset was refined using Coot[40], Refmac5 (Ref. 37) and Phenix[41]. The structure is deposited to the Protein Data Bank under the accession number 5CES. The resultant model of the C-terminus fragment was then used in combination with the cryoEM derived structure to build the final model of PA0618.

## Cryo electron microscopy

An aliquot of 2.5 μL of the above purified pyocin sample was loaded onto a "baked"[43] Quantifoil 1.2/1.3m, 200 mesh grid, blotted for 4 seconds at force 1, then flash-frozen with a Vitrobot Mark IV (FEI). CryoEM data were collected as movies in an FEI Titan Krios microscope (operated at 300kV) equipped with a Gatan imaging filter (GIF) (the slit was not inserted) and K2 Summit direct electron camera in counting mode using *Leginon* software package[44] for automation. Target defocus value is set to 2.0 μm under focus. Each movie contains 50 frames with 5 frames per second with a total accumulated dosage of 60 electrons per $Å^2$. The dose rate is measured at 6 electrons per $Å^2$ per second in the Digital Micrograph software package.

Frames within each movie were aligned to correct for drift as previously described[45], except that an iterative alignment scheme as previously described elsewhere[46] was used in addition to the original software. We output three averages of selected frames: $1^{st}$ to $50^{th}$ frames for particle selection, $3^{rd}$ to $20^{th}$ frames for refinement, and $3^{rd}$ to $13^{th}$ frames for final reconstruction.

The contrast transfer function (CTF) parameters of these movies were determined from the averages with $1^{st}$ to $50^{th}$ frames by *CTFFIND3* (Ref. 47). The range for acceptable defocus values was set to be between 1–3 μm, whereas outliers were rejected.

## Image processing and 3D reconstruction

As shown in Figure 1b, particles at both pre- and post-contraction states are present in the cryoEM images and can be readily distinguished by eye. The two ends of each pyocin were manually selected as individual particles with *EMAN*[48] *boxer* and were kept together prior to 3D classifications (see below). The box size for these particles is 320 and 420 pixels for the pre- and post-contraction states, respectively; and their total numbers of particles are 43,934 and 36,116, respectively. The trunk portion of each pre-contraction pyocin was boxed with *EMAN*[48] *helixboxer* with a box width of 384 and was segmented according to a 10% overlapping scheme, a total of 15,684 segments selected. Because the both ends of the post-contraction state contained sufficient structural components from the trunk, we did not pursue a helical reconstruction for the trunk in post-contraction state. Throughout these particle boxing processes, we only boxed particles that were not overlapping, not broken and not ice-contaminated.

Further image processing steps were performed with *Relion v1.2* (Ref. 49). The boxed particles were subjected first to 2D classification to eliminate poor particles and were then to a 3D classification to separate the collar and baseplate for each state (6 classes for pre-contraction state and 12 classes for post-contraction state). After separation of collar and baseplate, for each end of a pyocin particle and for each state, a further 3D classification was done to again eliminate poor particles (5 classes for pre-contraction baseplate, 8 classes for the rest).

The 3D models for the classes after this classification appeared to be mutually shifted along the particle axis. Therefore, the 3D model for all good classes are aligned to the one in the middle. The resulting shifts were projected to the 2D space of the original particles and were applied to the particle centers. The particles of the good classes were then extracted again using the translated coordinates.

The finally selected and re-extracted particles for each of the four structures were subjected to an auto-refinement in *Relion v1.2*. A 6-fold rotational symmetry was applied to the reconstructions. The number of finally included particles are as follows: pre-contraction collar: 4,109; pre-contraction baseplate: 26,104; post-contraction collar: 9,934; post-contraction baseplate: 15,582. The overall averaged resolutions of these final structures are estimated by ResMap[50] to be: pre-contraction collar: 3.9 Å; pre-contraction baseplate: 3.4 Å; post-contraction collar and baseplate: 3.5 Å (Extended Data Fig. 1).

## Protein subunit identification and atomic modeling

A purified pyocin preparation was run 5 mm into a 10% SDS gel and stained with coomassie blue. Each band containing a pyocin protein was excised, digested in-gel with trypsin, and subjected to liquid chromatography tandem mass spectrometry for sequencing analysis (conducted at the University of California Davis Proteomics Core). Proteins were then identified by comparing the mass spectrometry sequence fragments to the Pseudomonas aeruginosa PAO1 sequence (Extended Data Table 3 and Fig. 1e).

Atomic models were built *ab initio* with *Coot*[40]. We had to assign each of the above-identified protein candidates to a specific region in our cryoEM density map. At 3.4-Å resolution, this is possible because our map has sufficient resolving power for chain tracing and identification of side chains (Fig. 1c and Extended Data Fig. 2). For each peptide chain, we meticulously compared its secondary structure to the secondary structure predictions of all candidate proteins and found the best match. Once the match was found, the sequence of the candidate protein was compared to the amino acid side chain features in the density map to register the sequence. Then the alpha-carbon positions were manually traced with the above identified sequence in mind for each of the 11 unique atomic models. The alpha carbon trace was converted to a poly-alanine strand, and finally mutated to the correct amino acid sequence. Each of the side chains were manually inspected and fitted into the density along with additional attention to secondary structure conformations. Protein subunits were assembled into an asymmetric unit. Only protein subunits in one asymmetric unit were built. Symmetry-related copies were generated using the “sym” command in *UCSF Chimera*[51] with C6 rotational symmetry.

### Real-space model refinement

We carried out model refinement with the *phenix.real_space_refine* command of the *Phenix* package[41] using default settings in three steps. First, we refined each monomer model with the corresponding density cryoEM map individually. Second, we combined all the monomers in an asymmetric unit and refined it with the whole cryoEM map in order to separate clashing atoms between adjacent monomers within the asymmetric unit. Third, the refined model of the asymmetric unit was used to generate the full model of either the baseplate or collar using the "sym" command in *UCSF Chimera* with C6 rotational symmetry. This full model was refined globally with the NCS restraints enabled to separate clashing atoms among asymmetric units. At each of the refinement steps, we manually inspected the models to assess quality of the refinement, made manual adjustments and repeated the refinement steps until a final structure was reached. The refined models of the individual monomers and the full baseplate and collar were validated exhaustively with *EMRINGER* Score[52], Ramachandran Plot, C-beta, and map CC as well as *MolProbity*[53] and the results are tabulated in Extended Data Figure 1.

### Structure-based mutagenesis for PA0618

Mutations in the pyocin gene cluster were made in *P. aeruginosa* strain PAO1 by two-step allelic exchange following the method described in ref. 4. Briefly, ~1000 bp regions of DNA containing mutations were amplified from PAO1 genomic DNA using overlapping PCR and cloned into pEX18Gm (gift from Herbert Schweizer) that was digested with Kpn1 and EcoR1. The constructs were transformed by electroporation into PAO1 which was plated on 50 μg/ml gentamicin to select for single cross over integrants. Gentamicin resistant isolates were then picked, grown for 3 hrs in LB and plated on LB-sucrose plates to select for second crossover events. Colonies were picked and screened for gentamicin sensitivity. These were then sequence verified for correct mutations. Primers used for these constructs are shown in Supplementary Table 2.

Crude wildtype and H257F mutant pyocin were prepared as described above. Both were diluted 1:10 in either Tris buffer (10 mM Tris, 130 mM NaCl, pH 7.4) or phosphate-citrate buffer (28 mM $Na_2HPO_4$, 36 mM citric acid, pH 3.4) to adjust the pH. CryoEM imaging was done for each of the four resulting samples as described above. The numbers of pre-contraction and post-contraction pyocins were counted through visual inspection of about 200 images for each condition and their percentages were tallied in the bar graph in Figure 3f.

### PA0626 mutant construction

PA0626 mutants 626TEV and 626ΔWL were made using modified allelic exchange approach[54]. In brief, the whole WT R2-pyocin gene cluster resided on a pETcoco-1-based plasmid pSW192. In each case, two overlapping ~1 kb long fragments carrying the mutation were amplified using pSW192 as a template by the primers listed in Supplementary Table 2.

The donor vectors for the exchange pAK6 and pAK20 were assembled of pairs of fragments by NEBuilder reaction (New England Biolabs) on the backbone of pWM91 plasmid[55] in which the ampicillin resistance gene was replaced with the kanamycin resistance gene. The

recipient plasmid pSW192 was maintained in RecA+ *E. coli* 4s strain[56]. The donor vectors were transformed into MFDpyr *E. coli* strain[57] and conjugation between the donor and the acceptor strains was performed on LB agar plates overnight at 37°C. Selection for recombination products pSW192:pAK6 and pSW192:pAK20 was done on LB agar plates supplemented with kanamycin at 50 μg/ml. Counterselection for excision products, pSW192 and a mutation carrying plasmid, was done on agar plates with 1% trypton, 0.5% yeast extract and 5% sucrose (MilliporeSigma) overnight at room temperature. Colony screening was done by PCR. Plasmid identities were confirmed by sequencing.

### 626TEV in vivo digestion

For coexpression of pyocins with TEV protease, pS626TEV and pBAD24-based plasmid $pB^{h}$TEV coding TEV protease under the control of arabinose-inducible promoter were cotransformed into *E. coli* BL21ΔAraΔFhuA strain alongside with all necessary control combinations (WT pyocin coding plasmid pSW192 and $pB^{h}$TEV, pSW192 and pBAD24, pS626TEV and pBAD24). Clones were selected on agar plates for ampicillin and chloramphenicol resistance, grown in liquid LB medium supplemented with ampicillin at 100 μg/ml and chloramphenicol with 10 μg/ml at 37°C, induced with arabinose (0.01 and 0.03%) and incubated overnight at 30°C. Fresh lysates were cleared from debris for 5 minutes at 15000 g in a microcentrifuge, tested for killing activity on *P. aeruginosa* 13s strain lawns[58] in a spot assay and visualized on a JEOL-2100 electron microscope after staining with 2% uranyl acetate.

### Recombinant pyocin production

One liter of *E. coli* BL21ΔAraΔFhuA freshly transformed with each plasmid carrying wildtype or mutant pyocin gene clusters was grown in Lennox LB medium (Invitrogen) supplemented with chloramphenicol (11 μg/ml) in a 4 L erlenmeyer flask at 37°C and 240 rpm to an optical density of 1.0 at 600 nm. To induce pyocin expression, 0.5 ml of 20% arabinose were added, the temperature was decreased down to 30°C, and cells were incubated overnight. To get rid of debris and residual bacteria, the lysate was centrifuged at 15000 g for 30 minutes in a F9–6x-1000 rotor (Thermo Fisher Scientific). The lysate was supplemented with 4 mg of DNAse I and 4 mg of RNAse A (MilliporeSigma). 30 g of solid NaCl and 100 g of PEG 8000 (Fisher Scientific) were added and dissolved and the lysate was incubated at 4°C overnight to ensure the full precipitation of pyocins. Pyocins were pelleted at 15000 g for 15 minutes in a F9–6×1000 rotor and pellets were resuspended in 10 ml of SM buffer (8 mM $MgCl_2$, 100 mM NaCl, 50 mM Tris-HCl pH 7.5) with DNAse I and RNAse A at 1 μg/ml each. The sample were extracted with 10 ml of chloroform, centrifuged in 50 ml falcon tubes at 15000 g for 15 minutes. The pyocin containing aqueous phase was collected and pyocins were pelleted at 100000 g for 1 hr in a Type 70 Ti rotor (Beckman Coulter). The pellet was dissolved in 0.5 ml of SM buffer with shaking at 100 rpm overnight at 4°C. The sample was cleared from non-dissolvable material via centrifugation at 15000 g for 5 min in a microcentrifuge at room temperature and loaded on a step gradient of 10, 20, 30, 40 and 50% sucrose (0.9 ml each) and centrifuged at 100000 g for 1 hr in a SW 55 Ti rotor (Beckman Coulter). The upper pyocin containing band was isolated and dialysed against two changes of 0.1x SM buffer. The concentration of the dialysed sample was determined based on the adsorption at 280 nm and brought to 0.1 mg/ml. To get a control

sample of fully contracted pyocins, 20 μl of 3M Glycine-HCl pH 2.5 were added to 4 ml of normalized pyocin sample and contracted and non-contracted samples were dialysed against 10 mM NaCl 10 mM phosphate buffer pH 7.0. The whole procedure was repeated several times to get at least 3 independently prepared samples for each CD experiment performed.

### Circular dichroism

Pyocin contraction rates were measured on a JASCO J-815 CD spectrometer at 203 nm over a 67–74°C range with an increment of 1°C. Pyocin concentration for contracted and non-contracted samples maintained equal to 0.1 mg/ml in 10 mM NaCl 10 mM phosphate buffer pH 7.0. Each measurement took 25 min. Change of ellipticity for non-contracted pyocins were temperature dependent. It wasn't temperature dependent for contracted control samples. For data analysis, we averaged curves for each contracted sample and a resulting control curve subtracted from each contraction rate measurement of a cognate non-contracted sample. First two min of every measurement were trimmed as they correspond to a sample being heated up to desirable temperature and do not show pyocin contraction. Exponents were fitted into subtracted and trimmed data and the rate constants were determined with the help of MatLab CFTool (MathWorks). Arrhenius modeling of activation energy was also done in MatLab.

## Data Availability

CryoEM maps and the associated atomic models have been deposited to EMDB, PDB under the accession numbers EMD-20526/PDB:6PYT (pre-contraction helical trunk), EMD-20643/PDB:6U5B (pre-contraction baseplate), EMD-20646/PDB:6U5H (pre-contraction hub in C3 symmetry), EMD-20644/PDB:6U5F (pre-contraction collar), EMD-20647/PDB:6U5J (post-contraction collar) and EMD-20648/PDB:6U5K (post-contraction baseplate), respectively. X-ray crystal structures have been deposited to PDB under the accession numbers 5CES (PA0618 C-terminal domain), 4S36 (PA0616 C-terminal domain) and 4S37 (full length PA0616). All other data are available from the corresponding authors upon reasonable request.

## Code Availability

Modified version of MotionCorr 1 is available on GitHub, licensed under GPLv3 (gepeng1983/motioncorr1exp). Relion 1.2 with helical reconstruction patch is available on GitHub, licensed under GPLv2 (gepeng1983/relion12exp). A later version of Relion (1.4) with the same patch is also available on GitHub (gepeng1983/relion14exp).

## Extended Data

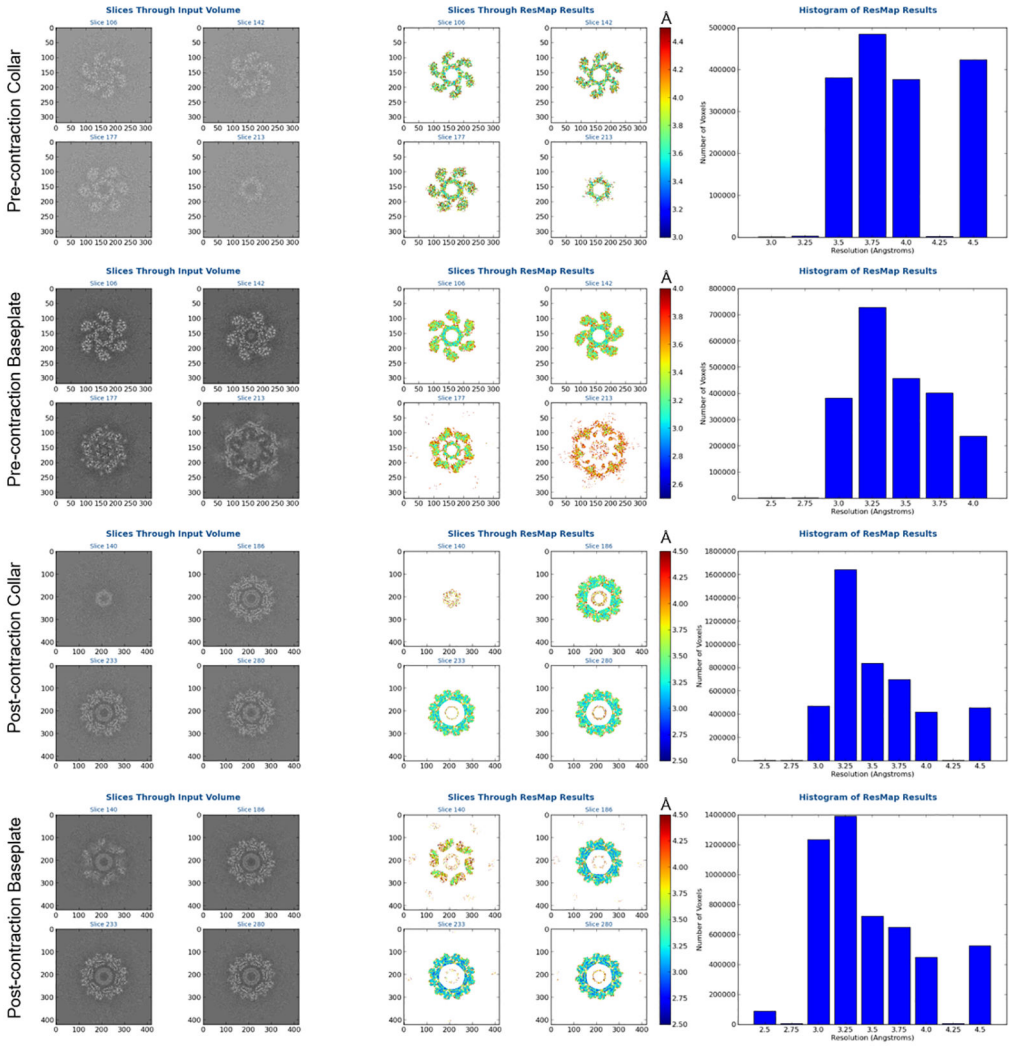


| Protein | | Ramachandran Outliers | Ramachandran Favored | Rotamer outliers | C-beta outliers | Bonds RMSD | Angles RMSD | Map CC | EMRinger Score |
|---|---|---|---|---|---|---|---|---|---|
| PA0615 / Collar | | 0% | 90.9% | 0.0% | 0.0% | 0.007 | 1.111 | 0.75 | 2.35 |
| Baseplate Subunits | PA0617 | 0% | 92.8% | 0.0% | 0.0% | 0.006 | 0.925 | 0.82 | 2.62 |
| | PA0618a | 0% | 91.7% | 0.4% | 0.0% | 0.005 | 0.989 | 0.67 | 2.39 |
| | PA0618b | 0% | 92.8% | 0.4% | 0.0% | 0.005 | 0.920 | 0.73 | 2.01 |
| | PA0619 | 0% | 91.3% | 0.0% | 0.0% | 0.005 | 1.040 | 0.71 | 2.54 |
| | PA0626 | 0% | 91.5% | 0.0% | 0.0% | 0.006 | 0.965 | 0.82 | 3.26 |
| | PA0627 | 0% | 94.3% | 0.0% | 0.0% | 0.005 | 0.957 | 0.81 | 4.59 |
| Baseplate Average | | 0% | 92.1% | 0.2% | 0.0% | 0.005 | 0.967 | 0.77 | 2.35 |

**Extended Data Figure 1. Resolution assessment and model validation for the cryoEM structures.**
*Resmap* results for the collar and baseplate regions of the pyocin reconstructions in pre- and post-contraction states. Listed in the table are model validation statistics for the collar, baseplate subunits and average.

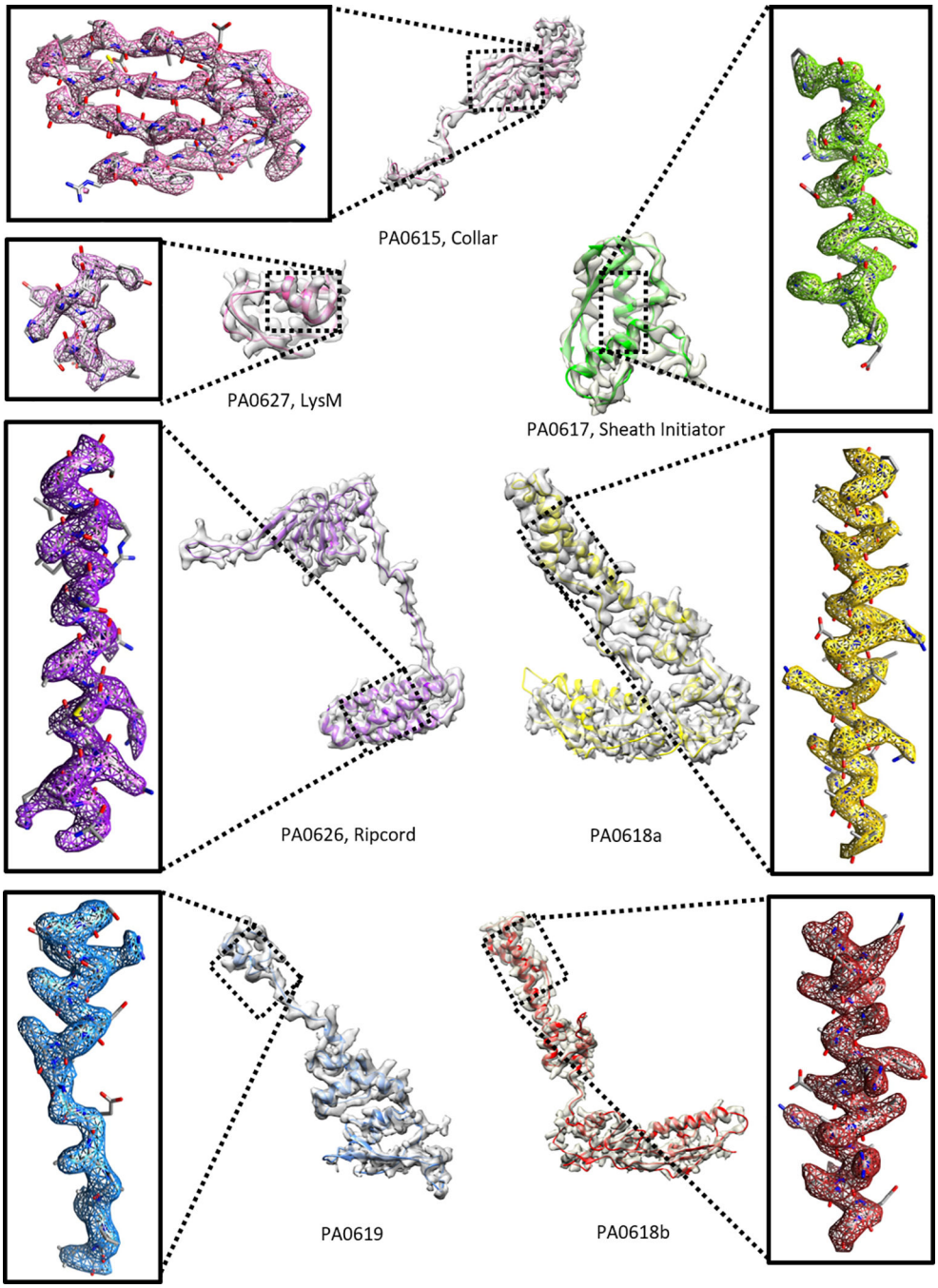


**Extended Data Figure 2. Model assessment of pre-contraction pyocin subunits.**

For each of the collar and baseplate proteins, the cryoEM density map is shown as semi-transparent gray superposed with its atomic model (ribbon). The close-up view of the box region shows the match of the density (wire-frames) and the atomic model (sticks).

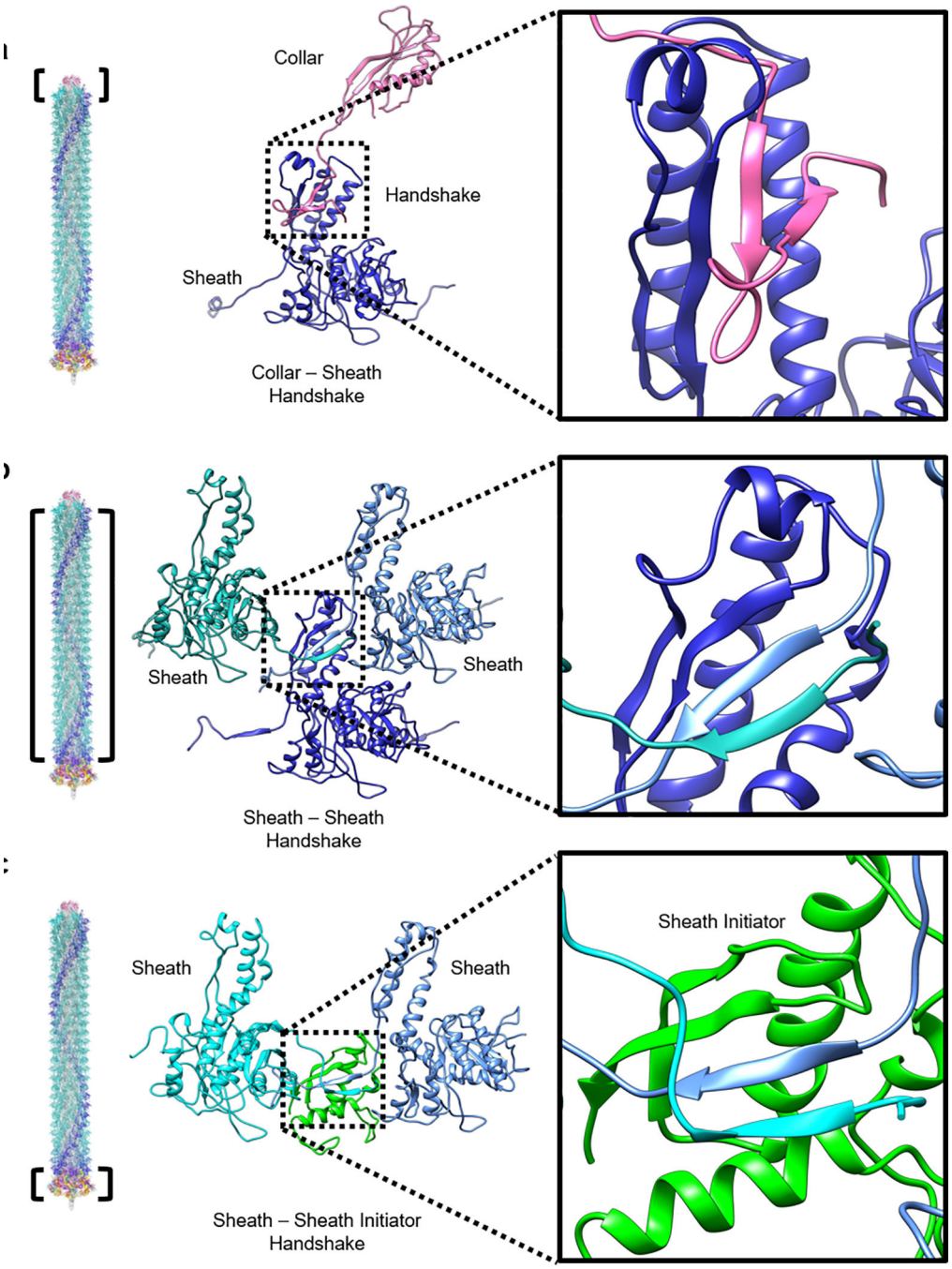


**Extended Data Figure 3. Types of sheath handshakes in pyocin.**

Ribbon diagrams depicting the 3 types of handshake conformations in pyocin: **a.** collar-sheath, **b.** sheath-sheath, and **c.** sheath-sheath initiator. All handshakes compose of a four-stranded β-sheet.

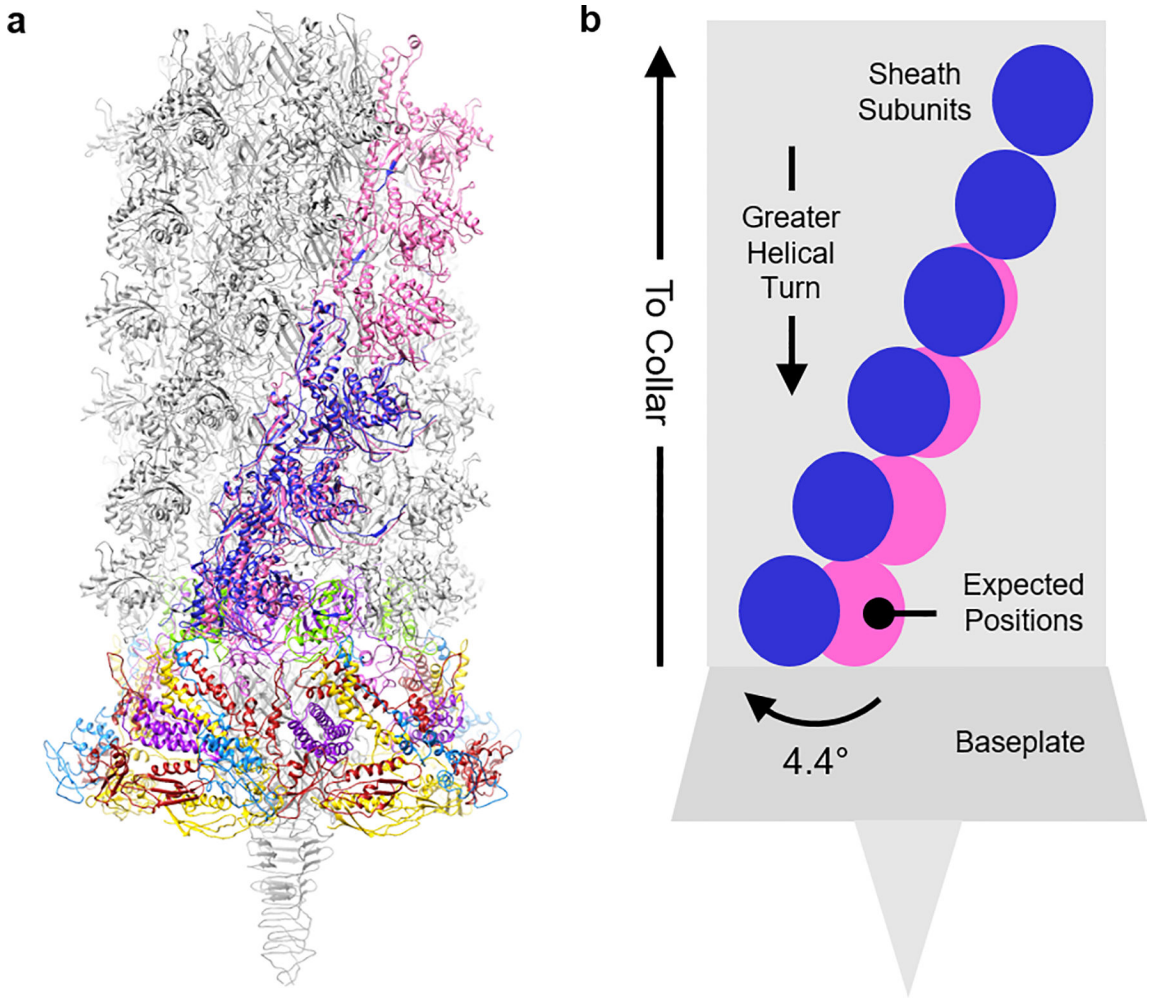


**Extended Data Figure 4. Trunk transitioning into baseplate.**

**a.** Ribbon diagram depicting lower portion of pyocin. **b.** Schematic diagram depicting changes in quaternary structure of the sheath subunits approaching the baseplate. The pink circles depict expected positions of the sheath subunits according to helical symmetry of trunk. The blue circles depict actual positions with greater sequential helical turn, 4.4° at the last disk of sheath.

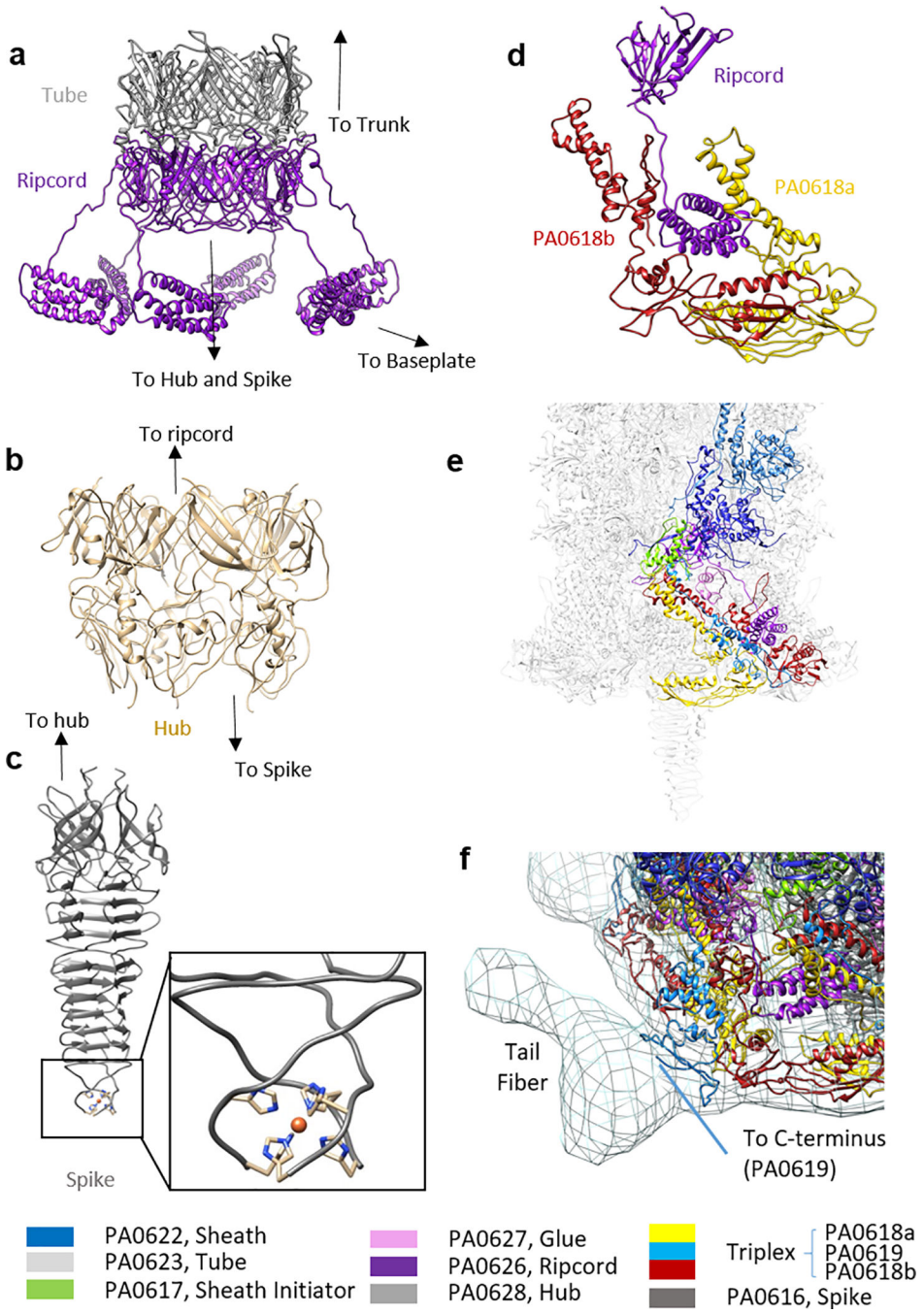


**Extended Data Figure 5. Inspection of the baseplate.**

**a.** Ribbon diagram of ripcord hexamer with tube hexamer. **b and c.** Ribbon diagram of the hub (**b**) and the spike (**c**) (with chelating site of its iron ion highlighted). **d**. Binding of ripcord into triplexes. **e**. Ribbon diagram of the baseplate with one sixth of its six-fold symmetric part highlighted in colors as in Fig. 1 showing relative positions of each subunit. **f.** Baseplate ribbon model superimposed with blurred cryoEM density map of the proximal region of the tail fiber.

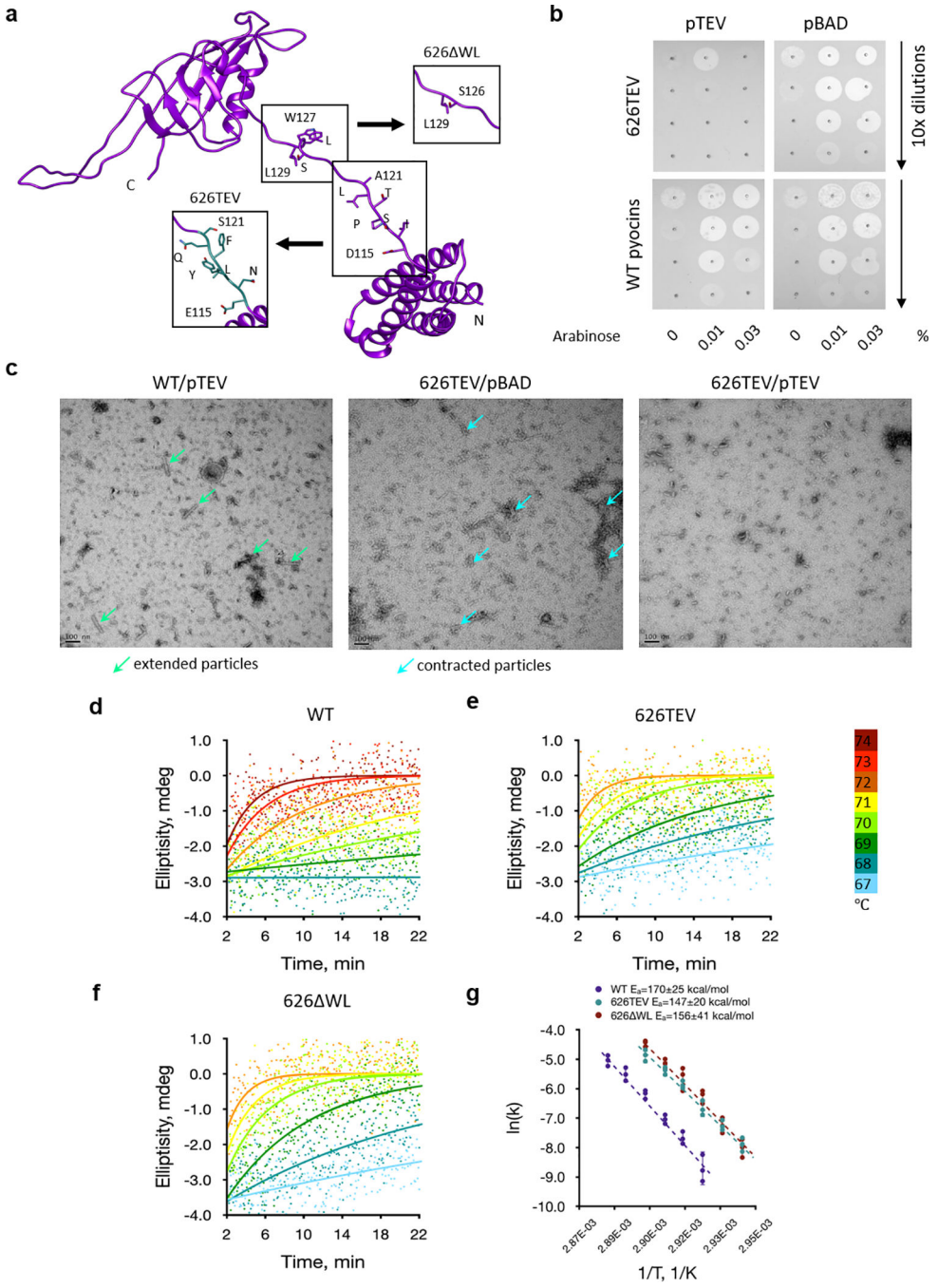


**Extended Data Figure 6. Functional and morphogenetic implications of ripcord mutagenesis.**

**a**. Overview of ripcord mutagenesis. **b**. Co-expression of the WT pyocin and mutant 626TEV with the TEV protease. Pyocin killing activity in the lysates was assessed with the help of a spot assay with *P. aeruginosa* 13s strain as prey. Both pyocin and protease expression levels are arabinose dependent with the rate of protease production being proportional to arabinose concentration and pyocin expression reaching the maximum at the lowest concentrations of arabinose tested (0.01%). Each experiment was repeated biologically three times, also for **c**-**g**. **c**. Representative negative staining electron

microscopy images of the crude lysates shown in the panel **b** induced with 0.01% arabinose. Despite showing killing activity in the lysates, no extended particles were found in the mutant 626TEV on EM grids. **d-f**. Temperature dependent sheath contraction rates of the WT pyocins and mutants measured with the help of circular dichroism. **g**. The rate constants $k(T)$ of WT pyocins, 626ΔWL and 626TEV fitted to the Arrhenius model $k(T) = A \exp(-E_a/RT)$ where $T$ is the absolute temperature, $A$ is a temperature independent constant, $E_a$ is the activation energy, $R$ is the ideal gas constant. The dots on the graph are individual values for three biologically independent measurements of $ln\ k(T)$, and the error bars show 95% confidence interval calculated for them.

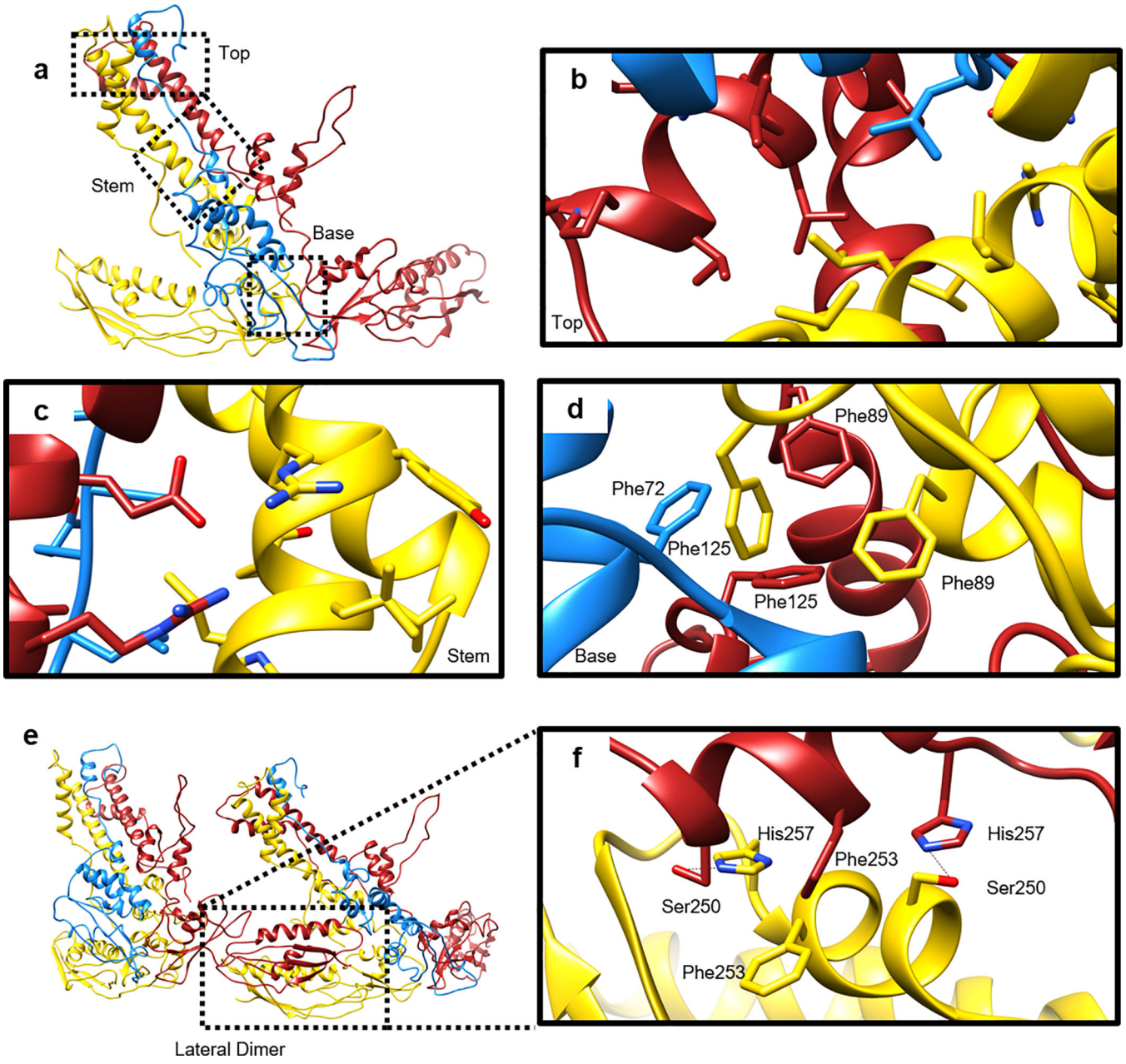

**Extended Data Figure 7. Interactions important for triplex formation.**

**a.** Ribbon diagram of the atomic model of the pyocin triplex. **b-d.** Ribbon model with depicted side chains in the top, stem, and base regions of the triplex. **d.** Phenylalanine pi-stacking coordination between PA0618a (yellow, Phe89, Phe125) PA0618b (red, Phe89, Phe125) and PA0619 (blue, Phe72). **e.** Ribbon model diagram of the lateral dimer. **f.** Close-up highlighting key interacting residues (Phe253 – Phe253, His257 – Ser250, Ser250 – His257).

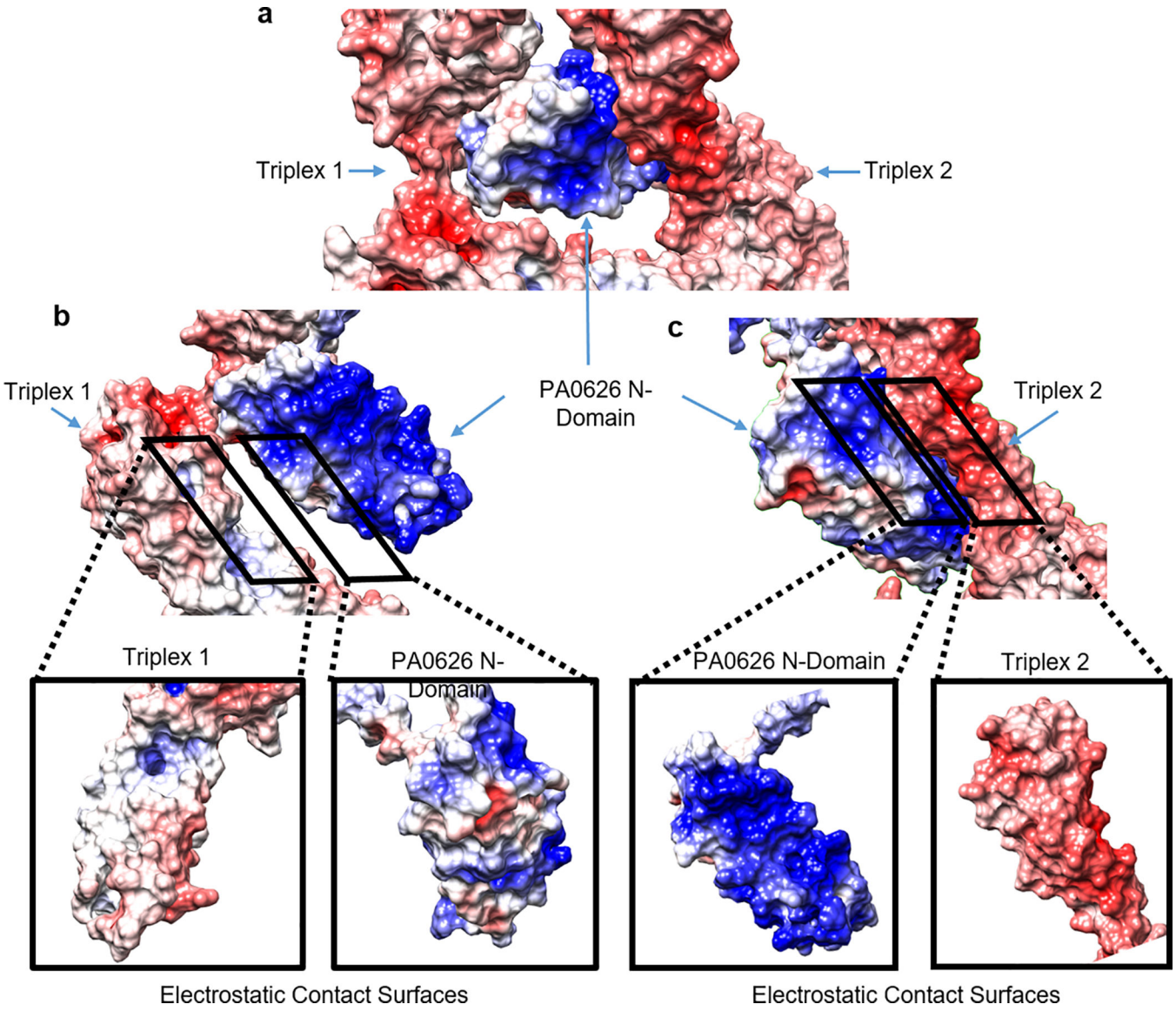


**Extended Data Figure 8. Electrostatic views of the ripcord handle.**

**a.** Electrostatic surface diagram of ripcord with adjacent triplexes. **b-c.** Electrostatic properties of the interfaces between ripcord and triplexes 1 and 2, respectively. Positive (blue), neutral (white), negative (red).

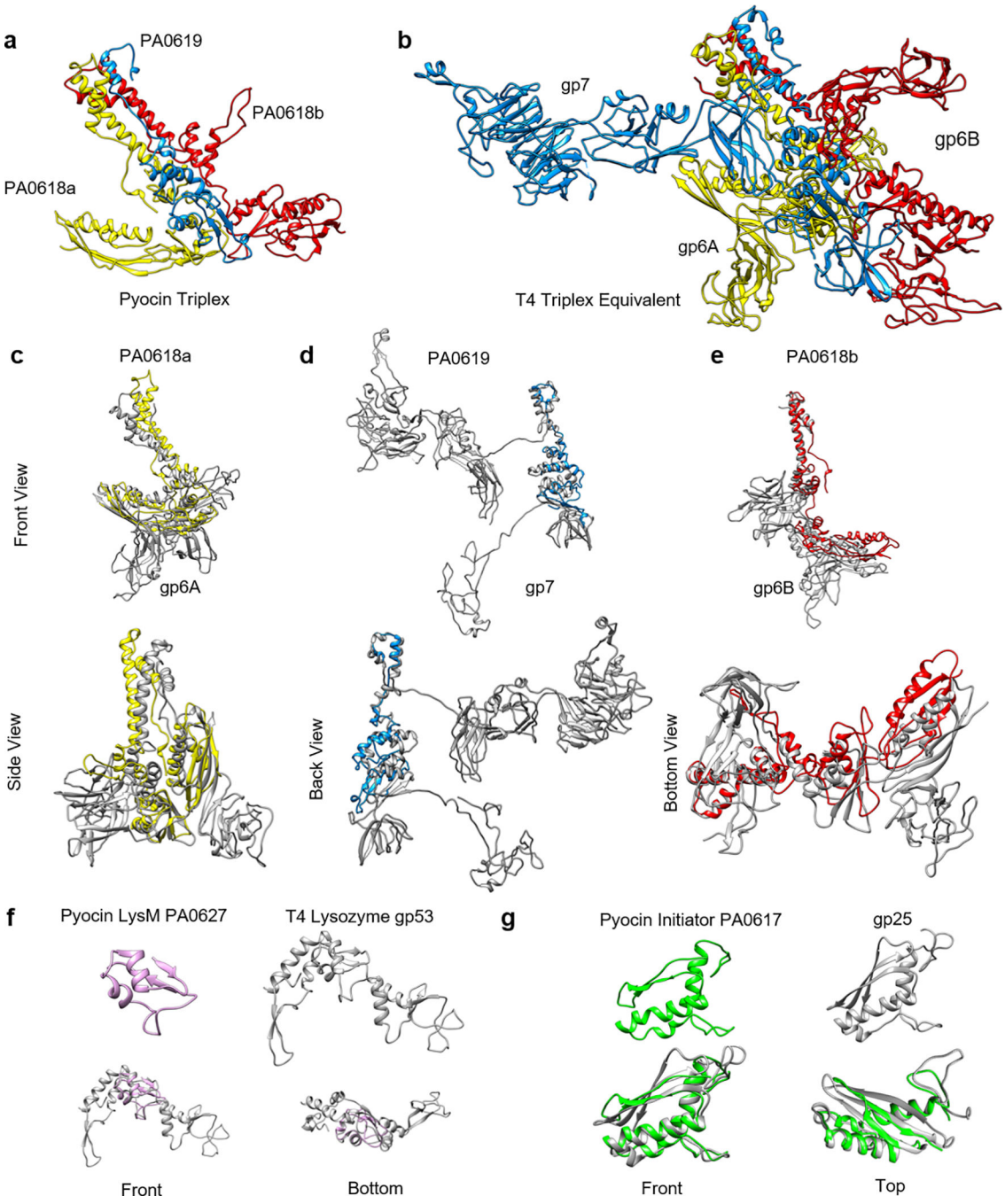


**Extended Data Figure 9. Comparison of related protein subunits from Pyocin R2 and T4 phage.**

Ribbon diagram of **a.** pyocin triplex, **b.** T4 triplex equivalent with subunits marked by corresponding color to (**a**), **c.** Pyocin PA0618a (yellow) and T4 gp6A (grey), **d.** Pyocin PA0619 (blue) and T4 gp7 (grey), **e.** Pyocin PA0618b (red) and T4 gp6B (grey), **f.** Pyocin PA0627 (pink) and T4 gp53 (grey), **g**. Pyocin PA0617 (green) and T4 gp25 (grey).

## Extended Data Table 1.

CryoEM data statistics.

| | Pre-contraction Trunk (EMDB-20526) (PDB 6PYT) | Pre-contraction Baseplate (EMDB-20643) (PDB 6U5B) | Pre-contraction Hub (C3 sym.) (EMDB-20646) (PDB 6U5H) | Pre-contraction Collar (EMDB-20644) (PDB 6U5F) | Post-contraction Collar (EMDB-20647) (PDB 6U5J) | Post-contraction Baseplate (EMDB-20648) (PDB 6U5K) |
|---|---|---|---|---|---|---|
| **Data collection and processing** | | | | | | |
| Magnification | 130,000 | 130,000 | 130,000 | 130,000 | 130,000 | 130,000 |
| Voltage (kV) | 300 | 300 | 300 | 300 | 300 | 300 |
| Electron exposure (e−/Å$^2$) | 30 | 30 | 30 | 30 | 30 | 30 |
| Defocus range (μm) | 1.2–3.4 | 1.2–3.4 | 1.2–3.4 | 1.2–3.4 | 1.2–3.4 | 1.2–3.4 |
| Pixel size (Å) | 1.07 | 1.07 | 1.07 | 1.07 | 1.07 | 1.07 |
| Symmetry imposed | C6 + helix | C6 | C3 | C6 | C6 | C6 |
| Initial particle images (no.) | 15,680 | 43,934 | 43,934 | 43,934 | 36,116 | 36,116 |
| Final particle images (no.) | 15,500 | 22,001 | 21,844 | 4,110 | 15,582 | 9,934 |
| Map resolution (Å) | 2.9 | 3.5 | 3.9 | 3.8 | 3.5 | 3.5 |
| FSC threshold | 0.143 | 0.143 | 0.143 | 0.143 | 0.143 | 0.143 |
| Map resolution range (Å) | 2.9–200 | 3.4–200 | 3.7–200 | 3.8–200 | 3.5–200 | 3.5–200 |
| **Refinement** | | | | | | |
| Initial model used (PDB code) | *de novo* | *de novo* | *de novo* | *de novo* | *de novo* | *de novo* |
| Model resolution (Å) | 3.1 | 3.4 | 4.0 | 3.7 | 3.5 | 3.5 |
| FSC threshold | 0.5 | 0.5 | 0.5 | 0.5 | 0.5 | 0.5 |
| Model resolution range (Å) | 2.9–200 | 3.4–200 | 3.7–200 | 3.8–200 | 3.5–200 | 3.5–200 |
| Map sharpening *B* factor (Å$^2$) | −80 | −80 | −80 | −80 | −80 | −80 |
| Model composition | | | | | | |
| Non-hydrogen atoms | 4,9920 | 103,392 | 7,326 | 107,550 | 59,634 | 110,142 |
| Protein residues | 6,624 | 13,608 | 954 | 14,232 | 7,878 | 14,520 |
| Ligands | 0 | 0 | 0 | 0 | 0 | 0 |
| *B* factors (Å$^2$) | | | | | | |

| | Pre-contraction Trunk (EMDB-20526) (PDB 6PYT) | Pre-contraction Baseplate (EMDB-20643) (PDB 6U5B) | Pre-contraction Hub (C3 sym.) (EMDB-20646) (PDB 6U5H) | Pre-contraction Collar (EMDB-20644) (PDB 6U5F) | Post-contraction Collar (EMDB-20647) (PDB 6U5J) | Post-contraction Baseplate (EMDB-20648) (PDB 6U5K) |
|---|---|---|---|---|---|---|
| Protein | 45.39 | 41.54 | 55.81 | 13.62 | 37.18 | 76.64 |
| Ligand | | | | | | |
| R.m.s. deviations | | | | | | |
| Bond lengths (Å) | 0.009 | 0.005 | 0.005 | 0.007 | 0.005 | 0.005 |
| Bond angles (°) | 1.000 | 0.941 | 1.054 | 0.999 | 0.700 | 0.770 |
| Validation | | | | | | |
| MolProbity score | 1.83 | 1.87 | 2.13 | 1.92 | 2.15 | 2.13 |
| Clashscore | 5.45 | 6.35 | 9.36 | 6.33 | 5.69 | 5.85 |
| Poor rotamers (%) | 0.94 | 0.17 | 0.39 | 0.38 | 3.03 | 3.00 |
| Ramachandran plot | | | | | | |
| Favored (%) | 90.48 | 91.13 | 86.41 | 89.01 | 93.32 | 92.97 |
| Allowed (%) | 9.52 | 8.87 | 13.59 | 10.99 | 7.68 | 7.03 |
| Disallowed (%) | 0.00 | 0.00 | 0.00 | 0.00 | 0.00 | 0.00 |

## Extended Data Table 2.

Crystallographic data statistics.

| Dataset name* | PA0618C $HoCl_2$ | PA0618C | PA0616d | PA0616 |
|---|---|---|---|---|
| **Data collection** | | | | |
| Space group | $P4_3$ | $P4_3$ | $P6_322$ | $P2_1$ |
| Cell dimensions: | | | | |
| a, b, c (Å) | 102.67, 102.47, 45.76 | 72.61, 72.61, 46.52 | 46.68, 46.68, 144.55 | 94.56, 137.052, 164.44 |
| α, β, γ (°) | 90.00, 90.00, 90.00 | 90.00, 90.00, 90.00 | 90.00, 90.00, 120.00 | 90.00, 106.88, 90.00 |
| Wavelength (Å) | 1.5352 | 0.91963 | 0.9763 | 1.6984 |
| Resolution (Å) | 50.0 – 2.80 (2.97 – 2.80)# | 50.0 – 2.10 (2.23 – 2.10) | 50.0 – 1.46 (1.55 – 1.46) | 50.0 – 2.20 (2.33 – 2.20) |
| $R_{meas}$ (%) | 9.7 (58.3) | 3.2 (73.6) | 3.4 (53.4) | 6.5 (95.2) |
| $CC_{1/2}$ | 99.9 (91.5) | 100.0 (81.8) | 100.0 (98.4) | 99.8 (83.2) |
| $I/\sigma_I$ | 25.35 (4.65) | 30.41 (2.61) | 56.52 (5.35) | 12.70 (1.33) |
| Completeness (%) | 99.2 (96.3) | 99.6 (97.8) | 99.6 (97.7) | 97.1 (92.3) |
| Redundancy | 13.9 (13.5) | 6.9 (6.7) | 21.8 (16.0) | 3.21 (2.95) |
| Anomalous signal$ | 1.770 (0.863) | | | |
| **Refinement** | | | | |

| **Dataset name*** | **PA0618C $HoCl_2$** | **PA0618C** | **PA0616d** | **PA0616** |
|---|---|---|---|---|
| Software (version) | | Phenix_refine (1.9_1692) | Phenix_refine (1.8.2_1309) | Phenix_refine (1.8.2_1309) |
| Resolution (Å) | | 50.0 – 2.10 | 50.0 – 1.46 | 50.0 – 2.20 |
| No. unique reflections | | 27,538 | 16,615 | 203,160 |
| No. atoms | | | | |
| Protein | | 1,403 | 744 | 23,767 |
| Ligand/ion | | 0 | 1 | 238 |
| Water | | 58 | 118 | 2,432 |
| *Rwork / Rfree* | | 0.190 / 0.236 | 0.149 / 0.188 | 0.163 / 0.208 |
| B-factors: | | | | |
| Protein ($Å^2$) | | 74.92 | 28.64 | 54.02 |
| Ligand/ion ($Å^2$) | | n/a | 24.51 | 117.84 |
| Water ($Å^2$) | | 68.68 | 46.50 | 55.16 |
| R.m.s. deviations | | | | |
| Bond lengths (Å) | | 0.003 | 0.008 | 0.004 |
| Bond angles (°) | | 0.705 | 1.274 | 0.889 |
| Ramachandran plot: | | | | |
| Favored (%) | | 97.77 | 98.86 | 96.03 |
| Allowed (%) | | 2.23 | 0.0 | 3.47 |
| Outliers (%) | | 0.0 | 1.14 | 0.50 |
| **PDB code** | | **5CES** | **4S36** | **4S37** |

*A single crystal was used for each of the datasets.

#The statistics for the highest resolution shell are given in parenthesis.

$As calculated by the program XDS (http://xds.mpimf-heidelberg.mpg.de/).

**Extended Data Table 3:**

Pyocin Protein Identification by Mass Spectrometry

| **MW (kDa)** | **Amino Acids** | **Gene Number (prf)** | **Gene Number (PA)** | **Copies (of monomer)** |
|---|---|---|---|---|
| 7.5 | 68 | 22 | PA0627 | Unknown |
| 11.8 | 108 | 12 | PA0617 | 6–18 |
| 18.1 | 168 | 18 | PA0623 | 100–200 |
| 18.9 | 171 | 10 | PA0615 | Unknown |
| 19.4 | 185 | 11 | PA0616 | 6–18 |
| 20.0 | 177 | 14 | PA0619 | Unknown |
| 31.3 | 290 | 21 | PA0626 | 6–18 |
| 32.0 | 295 | 13 | PA0618 | 6–18 |
| 35.9 | 329 | 23 | PA0628 | 6–18 |
| 41.2 | 386 | 17 | PA0622 | 100–200 |
| 77.7 | 745 | 20 | PA0625 | 1 |

## Supplementary Material

Refer to Web version on PubMed Central for supplementary material.

## Acknowledgements

We thank Xuekui Yu for advice in sample purification, UCLA students Kevin Wang, Lisa Nguyen, Regina Chi, Nicole Poweleit and Paul Graybeal and Beverly Hills High School student Johnathan Gunn and Laurie Wang for picking particles, UCLA student Emily Brown for video editing support, and David Martin of AvidBiotics for discussion and support throughout this project. This research was supported in part by NIH (R01GM071940 to ZHZ, R21AI085318 to DS), the Swiss National Science Foundation (31003A_146284 to PGL), and the Schaffer Family Foundation and Kavli Endowment (to JFM). Peng Ge was supported in part by American Heart Association Western States Affiliates Postdoc Fellowship (13POST17340020). We acknowledge the use of resources at the Electron Imaging Center for Nanomachines [EICN, supported by UCLA and by instrumentation grants from the NIH (1S10OD018111, 1U24GM11679) and NSF (DBI-1338135 and DMR-1548924)] and computation resource at the Extreme Science and Engineering Discovery Environment (XSEDE grant MCB140140 to ZHZ). Recharge fees for access to EICN facility for imaging the pyocin samples were partially defrayed by an award to ZHZ from the UCLA CTSI core voucher program.

## References

1. Ge P et al. Atomic structures of a bactericidal contractile nanotube in its pre- and postcontraction states. Nature structural & molecular biology 22, 377–382, doi:10.1038/nsmb.2995 (2015).
2. Scholl D Phage Tail-Like Bacteriocins. Annu Rev Virol 4, 453–467, doi:10.1146/annurev-virology-101416-041632 (2017). [PubMed: 28961412]
3. Scholl D et al. An engineered R-type pyocin is a highly specific and sensitive bactericidal agent for the food-borne pathogen Escherichia coli O157:H7. Antimicrob Agents Chemother 53, 3074–3080, doi:10.1128/AAC.01660-08 (2009). [PubMed: 19349519]
4. Williams SR, Gebhart D, Martin DW & Scholl D Retargeting R-type pyocins to generate novel bactericidal protein complexes. Appl Environ Microbiol 74, 3868–3876, doi:10.1128/AEM.00141-08 (2008). [PubMed: 18441117]
5. Taylor NM et al. Structure of the T4 baseplate and its function in triggering sheath contraction. Nature 533, 346–352, doi:10.1038/nature17971 (2016). [PubMed: 27193680]
6. Leiman PG et al. Type VI secretion apparatus and phage tail-associated protein complexes share a common evolutionary origin. Proc Natl Acad Sci U S A 106, 4154–4159, doi:10.1073/pnas.0813360106 (2009). [PubMed: 19251641]
7. Kudryashev M et al. Structure of the type VI secretion system contractile sheath. Cell 160, 952–962, doi:10.1016/j.cell.2015.01.037 (2015). [PubMed: 25723169]
8. Basler M, Pilhofer M, Henderson GP, Jensen GJ & Mekalanos JJ Type VI secretion requires a dynamic contractile phage tail-like structure. Nature 483, 182–186, doi:http://www.nature.com/nature/journal/v483/n7388/abs/nature10846.html#supplementary-information (2012). [PubMed: 22367545]
9. Leiman PG & Shneider MM Contractile tail machines of bacteriophages. Adv Exp Med Biol 726, 93–114, doi:10.1007/978-1-4614-0980-9_5 (2012). [PubMed: 22297511]
10. Clemens DL, Ge P, Lee BY, Horwitz MA & Zhou ZH Atomic structure of T6SS reveals interlaced array essential to function. Cell 160, 940–951, doi:10.1016/j.cell.2015.02.005 (2015). [PubMed: 25723168]
11. Bock D et al. In situ architecture, function, and evolution of a contractile injection system. Science 357, 713–717, doi:10.1126/science.aan7904 (2017). [PubMed: 28818949]
12. Ho BT, Dong TG & Mekalanos JJ A view to a kill: the bacterial type VI secretion system. Cell Host Microbe 15, 9–21, doi:10.1016/j.chom.2013.11.008 (2014). [PubMed: 24332978]
13. Mougous JD et al. A virulence locus of Pseudomonas aeruginosa encodes a protein secretion apparatus. Science 312, 1526–1530, doi:10.1126/science.1128393 (2006). [PubMed: 16763151]
14. Stover CK et al. Complete genome sequence of Pseudomonas aeruginosa PAO1, an opportunistic pathogen. Nature 406, 959–964, doi:10.1038/35023079 (2000). [PubMed: 10984043]

15. Aksyuk AA et al. The tail sheath structure of bacteriophage T4: a molecular machine for infecting bacteria. The EMBO Journal 28, 821–829 (2009). [PubMed: 19229296]
16. Kostyuchenko VA et al. The tail structure of bacteriophage T4 and its mechanism of contraction. Nat Struct Mol Biol 12, 810–813 (2005). [PubMed: 16116440]
17. Leiman PG, Chipman PR, Kostyuchenko VA, Mesyanzhinov VV & Rossmann MG Three-Dimensional Rearrangement of Proteins in the Tail of Bacteriophage T4 on Infection of Its Host. Cell 118, 419–429 (2004). [PubMed: 15315755]
18. Hu B, Margolin W, Molineux IJ & Liu J Structural remodeling of bacteriophage T4 and host membranes during infection initiation. Proc Natl Acad Sci U S A 112, E4919–4928, doi:10.1073/pnas.1501064112 (2015). [PubMed: 26283379]
19. Hu B, Margolin W, Molineux IJ & Liu J The bacteriophage t7 virion undergoes extensive structural remodeling during infection. Science 339, 576–579, doi:10.1126/science.1231887 (2013). [PubMed: 23306440]
20. Hatfull GF Bacteriophage genomics. Curr Opin Microbiol 11, 447–453, doi:10.1016/j.mib.2008.09.004 (2008). [PubMed: 18824125]
21. Hendrix RW, Hatfull GF & Smith MC Bacteriophages with tails: chasing their origins and evolution. Res Microbiol 154, 253–257, doi:10.1016/S0923-2508(03)00068-8 (2003). [PubMed: 12798229]
22. Chen Z et al. Cryo-EM structure of the bacteriophage T4 isometric head at 3.3-A resolution and its relevance to the assembly of icosahedral viruses. Proc Natl Acad Sci U S A 114, E8184–E8193, doi:10.1073/pnas.1708483114 (2017). [PubMed: 28893988]
23. Jiang F et al. Cryo-EM Structure and Assembly of an Extracellular Contractile Injection System. Cell 177, 370–383 e315, doi:10.1016/j.cell.2019.02.020 (2019). [PubMed: 30905475]
24. Desfosses A et al. Atomic structures of an entire contractile injection system in both the extended and contracted states. Nat Microbiol, doi:10.1038/s41564-019-0530-6 (2019).
25. Chang YW, Rettberg LA, Ortega DR & Jensen GJ In vivo structures of an intact type VI secretion system revealed by electron cryotomography. EMBO Rep 18, 1090–1099, doi:10.15252/embr.201744072 (2017). [PubMed: 28487352]
26. Hu B et al. Visualization of the type III secretion sorting platform of Shigella flexneri. Proc Natl Acad Sci U S A 112, 1047–1052, doi:10.1073/pnas.1411610112 (2015). [PubMed: 25583506]
27. Low HH et al. Structure of a type IV secretion system. Nature 508, 550, doi:10.1038/nature13081 (2014). [PubMed: 24670658]
28. Kirk JA et al. New class of precision antimicrobials redefines role of Clostridium difficile S-layer in virulence and viability. Sci Transl Med 9, doi:10.1126/scitranslmed.aah6813 (2017).
29. Ritchie JM et al. An Escherichia coli O157-specific engineered pyocin prevents and ameliorates infection by E. coli O157:H7 in an animal model of diarrheal disease. Antimicrob Agents Chemother 55, 5469–5474, doi:10.1128/AAC.05031-11 (2011). [PubMed: 21947394]
30. Browning C, Shneider MM, Bowman VD, Schwarzer D & Leiman PG Phage pierces the host cell membrane with the iron-loaded spike. Structure 20, 326–339, doi:10.1016/j.str.2011.12.009 (2012). [PubMed: 22325780]
31. Kageyama M, Ikeda K & Egami F Studies of a Pyocin. Iii. Biological Properties of the Pyocin. J Biochem 55, 59–64 (1964). [PubMed: 14116621]
32. Crawford JT & Goldberg EB The function of tail fibers in triggering baseplate expansion of bacteriophage T4. J Mol Biol 139, 679–690, doi:10.1016/0022-2836(80)90054-6 (1980). [PubMed: 6997499]
33. Gebhart D et al. A modified R-type bacteriocin specifically targeting Clostridium difficile prevents colonization of mice without affecting gut microbiota diversity. MBio 6, doi:10.1128/mBio.02368-14 (2015).
34. Scholl D, Gebhart D, Williams SR, Bates A & Mandrell R Genome sequence of E. coli O104:H4 leads to rapid development of a targeted antimicrobial agent against this emerging pathogen. PLoS One 7, e33637, doi:10.1371/journal.pone.0033637 (2012). [PubMed: 22432037]

## Additional References


35. Soding J, Biegert A & Lupas AN The HHpred interactive server for protein homology detection and structure prediction. Nucleic Acids Res 33, W244–248, doi:10.1093/nar/gki408 (2005). [PubMed: 15980461]
36. Vagin A & Teplyakov A Molecular replacement with MOLREP. Acta Crystallogr D Biol Crystallogr 66, 22–25, doi:10.1107/S0907444909042589 (2010). [PubMed: 20057045]
37. Murshudov GN et al. REFMAC5 for the refinement of macromolecular crystal structures. Acta Crystallogr D Biol Crystallogr 67, 355–367, doi:10.1107/S0907444911001314 (2011). [PubMed: 21460454]
38. Zhang KY, Cowtan K & Main P Combining constraints for electron-density modification. Methods Enzymol 277, 53–64, doi:10.1016/s0076-6879(97)77006-x (1997). [PubMed: 18488305]
39. McCoy AJ et al. Phaser crystallographic software. J Appl Crystallogr 40, 658–674, doi:10.1107/S0021889807021206 (2007). [PubMed: 19461840]
40. Emsley P, Lohkamp B, Scott WG & Cowtan K Features and development of Coot. Acta Crystallographica Section D 66, 486–501, doi:doi:10.1107/S0907444910007493 (2010).
41. Adams PD et al. PHENIX: a comprehensive Python-based system for macromolecular structure solution. Acta Crystallographica Section D 66, 213–221, doi:doi:10.1107/S0907444909052925 (2010).
42. Cowtan K The Buccaneer software for automated model building. 1. Tracing protein chains. Acta Crystallogr D Biol Crystallogr 62, 1002–1011, doi:10.1107/S0907444906022116 (2006). [PubMed: 16929101]
43. Miyazawa A, Fujiyoshi Y & Unwin N Structure and gating mechanism of the acetylcholine receptor pore. Nature 423, 949–955, doi:10.1038/nature01748 (2003). [PubMed: 12827192]
44. Suloway C et al. Automated molecular microscopy: the new Leginon system. Journal of Structural Biology 151, 41–60, doi:10.1016/j.jsb.2005.03.010 (2005). [PubMed: 15890530]
45. Li X et al. Electron counting and beam-induced motion correction enable near-atomic-resolution single-particle cryo-EM. Nat Methods 10, 584–590, doi:10.1038/nmeth.2472 (2013). [PubMed: 23644547]
46. Banerjee S et al. 2.3 A resolution cryo-EM structure of human p97 and mechanism of allosteric inhibition. Science 351, 871–875, doi:10.1126/science.aad7974 (2016). [PubMed: 26822609]
47. Mindell JA & Grigorieff N Accurate determination of local defocus and specimen tilt in electron microscopy. Journal of Structural Biology 142, 334–347 (2003). [PubMed: 12781660]
48. Ludtke SJ, Baldwin PR & Chiu W EMAN: semiautomated software for high-resolution single-particle reconstructions. J Struct Biol 128, 82–97 (1999). [PubMed: 10600563]
49. Scheres SHW RELION: Implementation of a Bayesian approach to cryo-EM structure determination. Journal of Structural Biology 180, 519–530, doi:10.1016/j.jsb.2012.09.006 (2012). [PubMed: 23000701]
50. Kucukelbir A, Sigworth FJ & Tagare HD Quantifying the local resolution of cryo-EM density maps. Nat Methods 11, 63–65, doi:10.1038/nmeth.2727 (2014). [PubMed: 24213166]
51. Pettersen EF et al. UCSF Chimera--a visualization system for exploratory research and analysis. J Comput Chem 25, 1605–1612 (2004). [PubMed: 15264254]
52. Barad BA et al. EMRinger: side chain-directed model and map validation for 3D cryo-electron microscopy. Nat Meth 12, 943–946, doi:10.1038/nmeth.354110.1038/nmeth.3541http://www.nature.com/nmeth/journal/v12/n10/abs/nmeth.3541.html#supplementary-informationhttp://www.nature.com/nmeth/journal/v12/n10/abs/nmeth.3541.html#supplementary-information (2015).
53. Chen VB et al. MolProbity: all-atom structure validation for macromolecular crystallography. Acta Crystallogr D Biol Crystallogr 66, 12–21, doi:10.1107/S0907444909042073 (2010). [PubMed: 20057044]
54. Blomfield IC, Vaughn V, Rest RF & Eisenstein BI Allelic exchange in Escherichia coli using the Bacillus subtilis sacB gene and a temperature-sensitive pSC101 replicon. Mol Microbiol 5, 1447–1457 (1991). [PubMed: 1686293]

55. Metcalf WW et al. Conditionally replicative and conjugative plasmids carrying lacZ alpha for cloning, mutagenesis, and allele replacement in bacteria. Plasmid 35, 1–13, doi:10.1006/plas.1996.0001 (1996). [PubMed: 8693022]

56. Prokhorov NS et al. Function of bacteriophage G7C esterase tailspike in host cell adsorption. Mol Microbiol 105, 385–398, doi:10.1111/mmi.13710 (2017). [PubMed: 28513100]

57. Ferrieres L et al. Silent mischief: bacteriophage Mu insertions contaminate products of Escherichia coli random mutagenesis performed using suicidal transposon delivery plasmids mobilized by broad-host-range RP4 conjugative machinery. J Bacteriol 192, 6418–6427, doi:10.1128/JB.00621-10 (2010). [PubMed: 20935093]

58. Scholl D & Martin DW Jr. Antibacterial efficacy of R-type pyocins towards Pseudomonas aeruginosa in a murine peritonitis model. Antimicrob Agents Chemother 52, 1647–1652, doi:10.1128/aac.01479-07 (2008). [PubMed: 18332164]

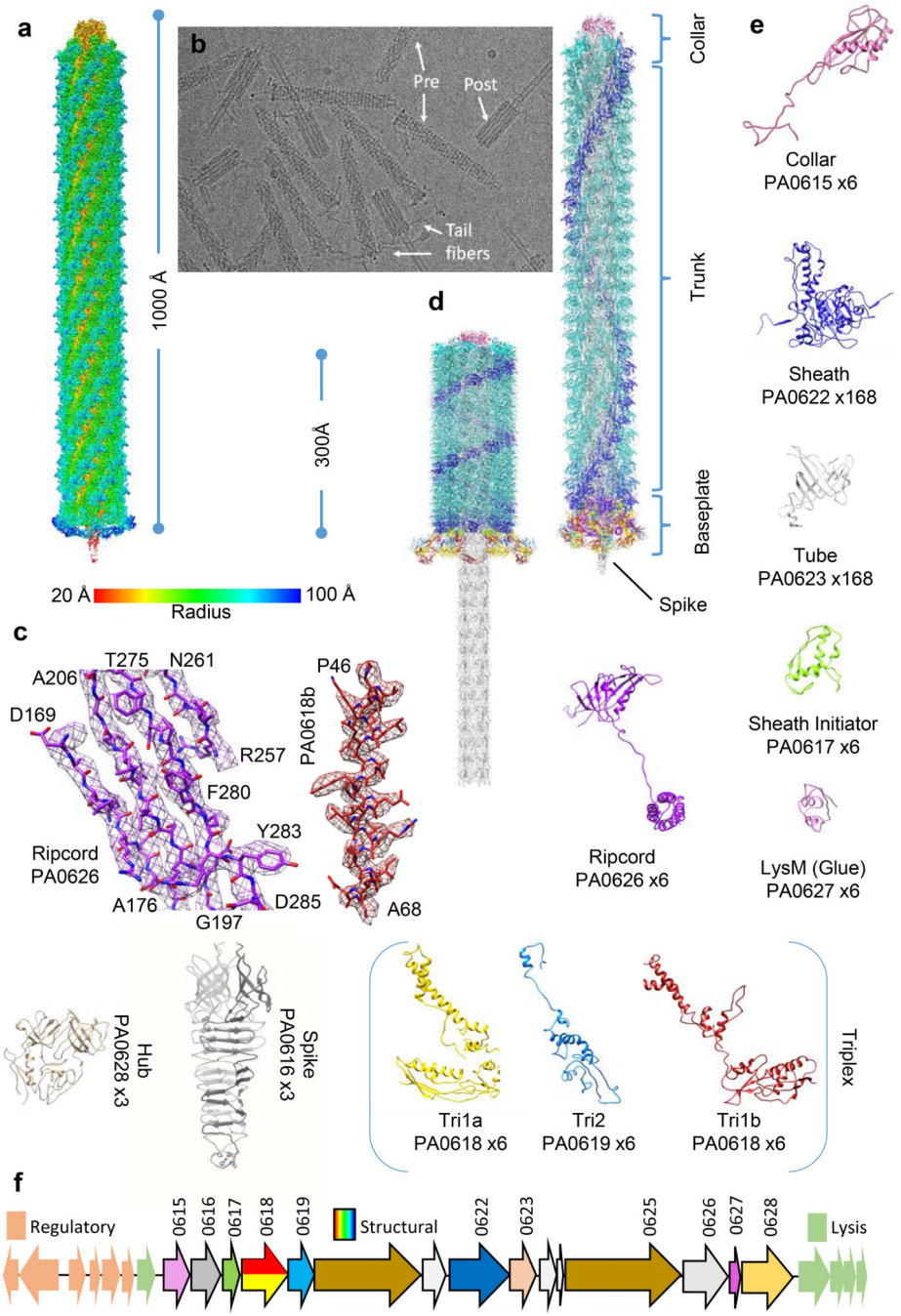


**Figure 1. CryoEM and overall structure of pyocin in pre- and post-contracted states.**

**a.** Shaded surface representation of the cryoEM reconstructions, colored according to cylindrical radii as shown in the color bar. **b.** Representative cryoEM micrograph. **c.** Regions of the cryoEM density map (mesh) superimposed with atomic models (sticks) demonstrating the agreement between the observed and modeled amino acid side chains. **d.** Atomic models for pyocin in both the pre- and post-contracted states. **e** and **f.** Ribbon diagrams of individual subunits of pyocin in the pre-contracted state (**e**) shown along with their corresponding gene loci (**f**). See 3 dimensional rendition in Supplementary Videos 1 to 3.

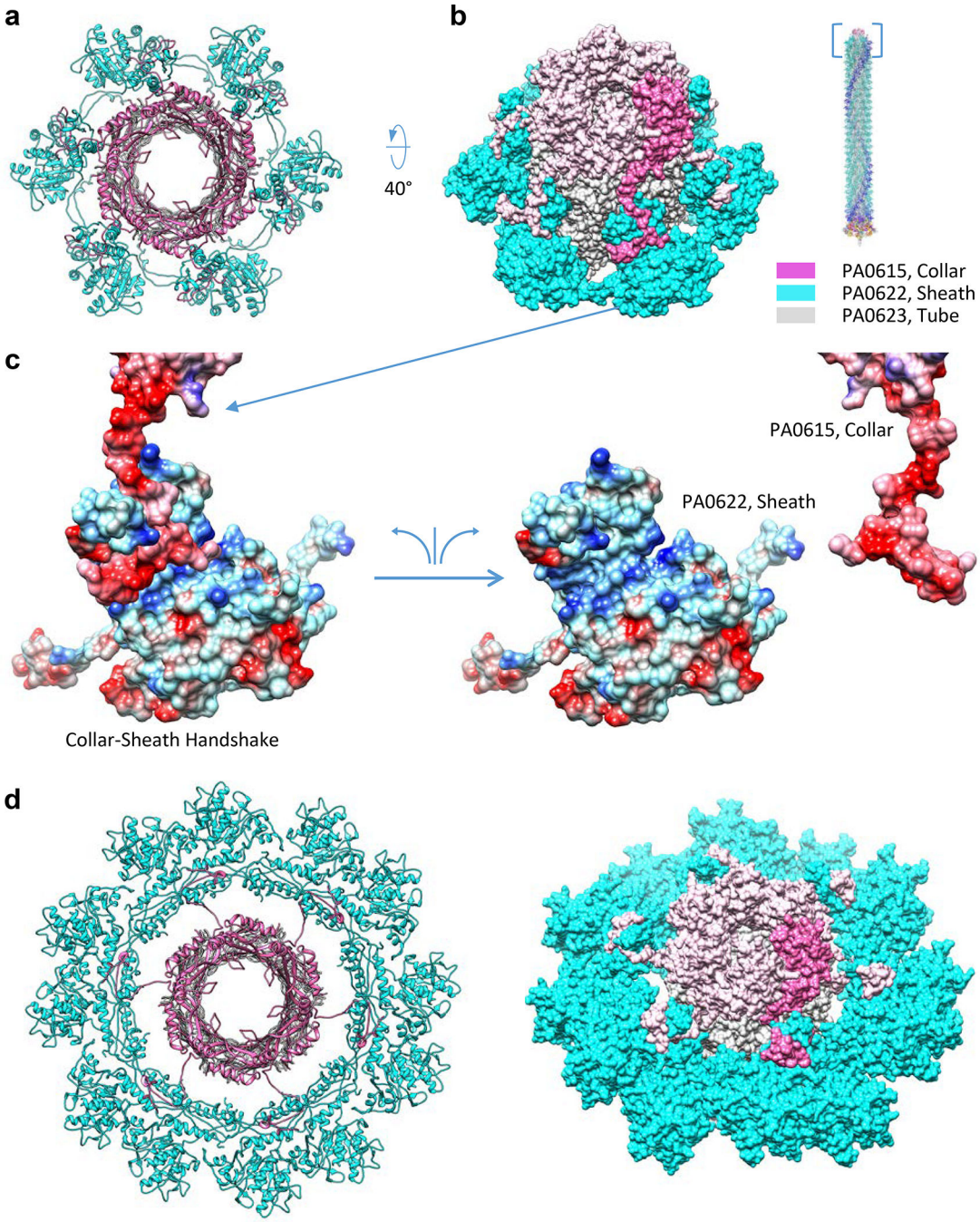


**Figure 2. Architecture of the collar.**

**a.** Top view ribbon diagram of the collar (pink), outer sheath (cyan) and inner tube (grey). **b.** Space filling model of collar-sheath-tube region. **c.** Electrostatic surface model of collar sheath handshake with views of the interacting charged surfaces. Positive (blue), negative (red), neutral (same as **b**). **d.** ribbon and space filling diagrams of the post-contraction collar-sheath-tube region similar to **a** and **b**.

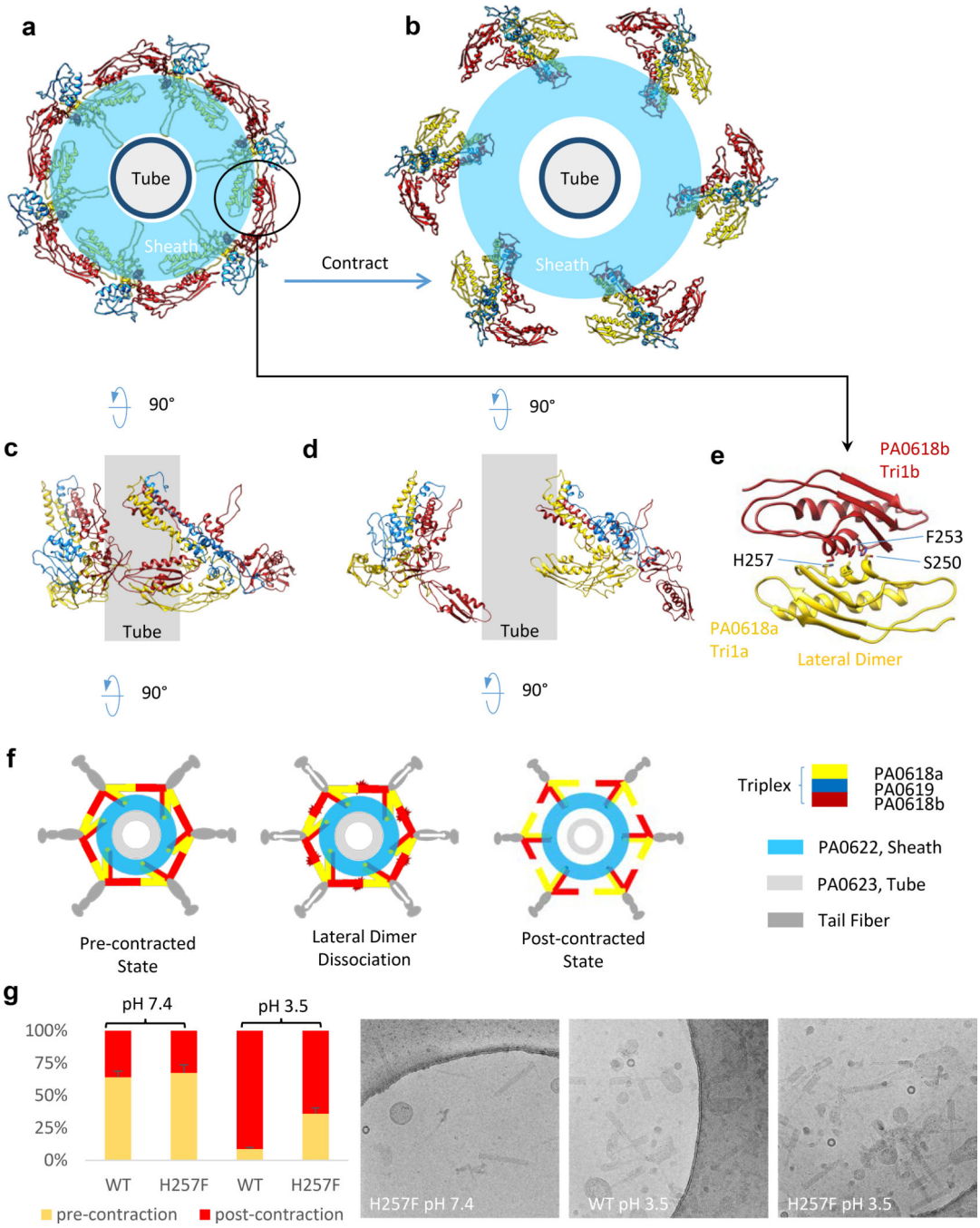


**Figure 3. Triplex expansion and lateral dimer dissociation.**

**a-e.** Ribbon diagrams of triplexes forming an iris ring in pre-contracted state (**a**), expanded iris in post-contracted state (**b**), side view of two adjacent triplexes in pre-contracted state (**c**) and post-contracted state (**d**), and lateral dimer of PA0618 (**e**). **f.** Schematic of the iris ring expansion as result of the tail fiber actuation. **g**. PA0618 H257F mutant. Left, percentages of pre-contraction pyocins in purified wildtype (WT) and H257F mutant under cryoEM at neutral and acidic pH. (pH 7.4 WT: 185/289, H257F: 118/175; pH 3.5 WT: 46/530, H257F:

64/178. Error bars: standard deviations.) Right, representative cryoEM image for each relevant condition.

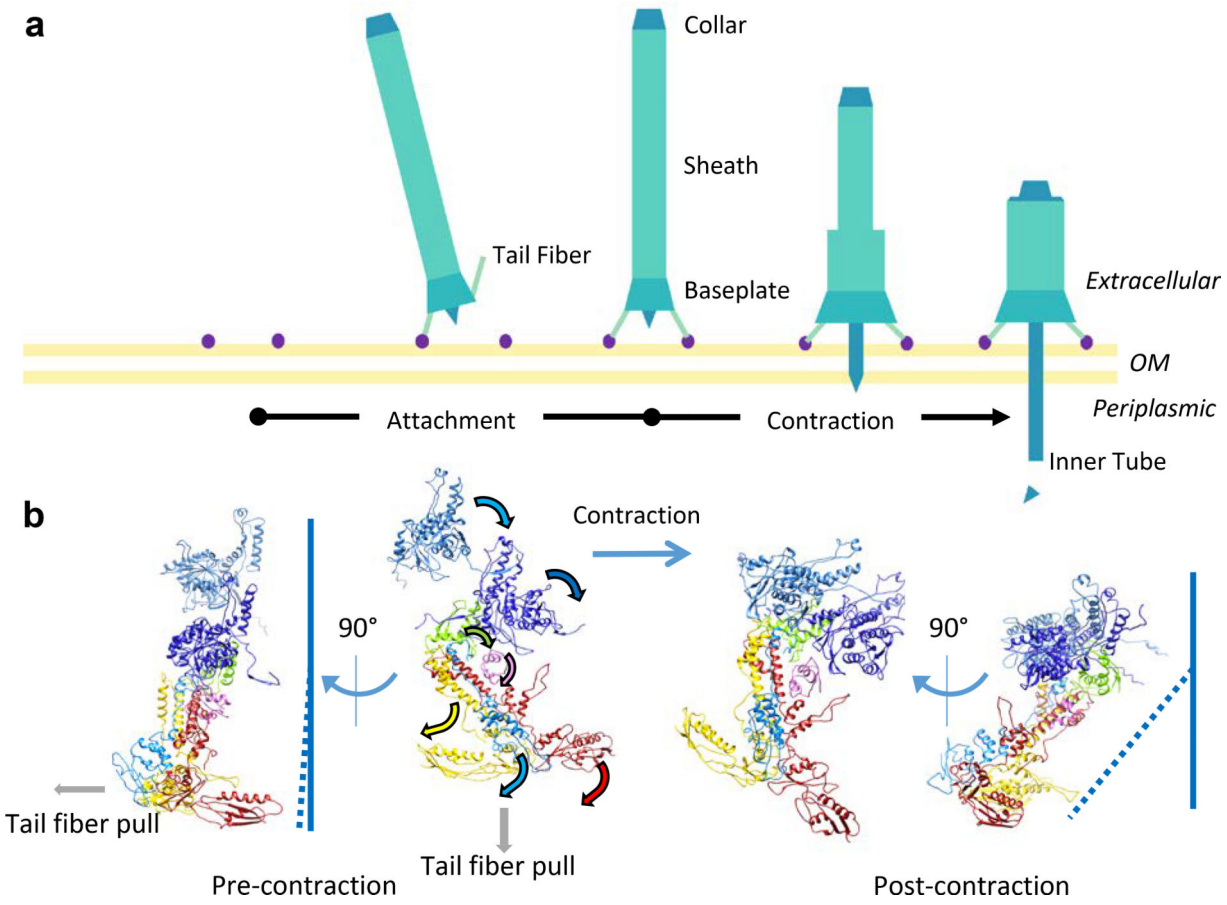


**Figure 4. Baseplate transition from the pre- to post-contracted state.**

**a.** Illustration of a pyocin landing on a bacterial cell and firing. Release of the spike and hub following injection is postulated on the basis of the lack of these structures on contracted particles that we observed *in vitro.* **b.** Ribbon diagram of the conserved baseplate components and sheath proteins in its pre- and post-contracted states. Ripcord is believed to travel with the inner tube during the power stroke and therefor is not a conserved component of the baseplate after contraction.